AD-A128 432 EFFECTS OF NONCONVECTIVE ELECTRIC FIELDS ON MAGNETOSPHERIC PLASMA DYNAMICS(U) NORTHEASTERN UNIV BOSTON MA M B SILEVITCH 31 JAN 83 AFOSR-TR-83-0379 1/2

UNCLASSIFIED AFOSR-78-3731 F/G 20/9 NL

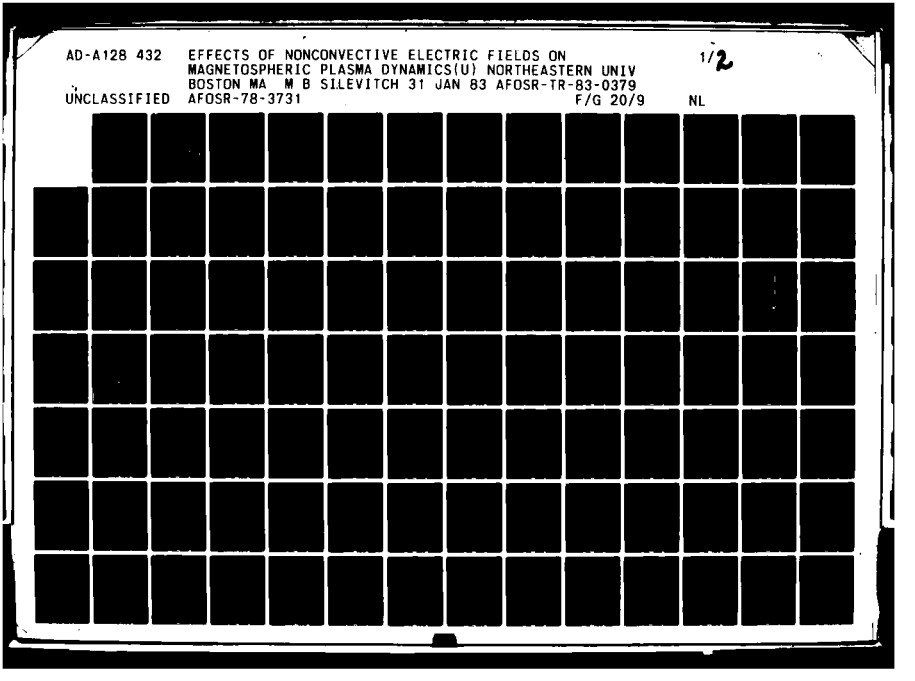

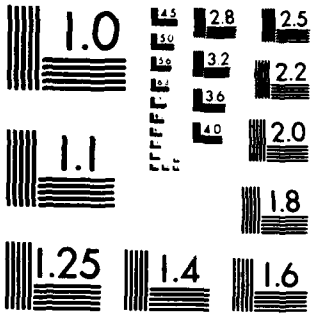

AFOSR-TR- 83 - 0379

(1)

FINAL REPORT

GRANT AFOSR 78-3731

Effects of Nonconvective Electric Fields on Magnetospheric Plasma Dynamics

UNCLASSIFIED

SECURITY CLASSIFICATION OF THIS PAGE (When Data Entered)

REPORT DOCUMENTATION PAGE		READ INSTRUCTIONS BEFORE COMPLETING FORM
1. REPORT NUMBER AFOSR-TR- 83 - 0379	2. GOVT ACCESSION NO. AD-A128 432	3. RECIPIENT'S CATALOG NUMBER
4. TITLE (and Subtitle) EFFECTS OF NONCONVECTIVE ELECTRIC FIELDS ON MAGNETOSPHERIC PLASMA DYNAMICS		5. TYPE OF REPORT & PERIOD COVERED Final 1 Dec 81 - 31 Jan 83
		6. PERFORMING ORG. REPORT NUMBER
7. AUTHOR(s) M. B. Silevitch		8. CONTRACT OR GRANT NUMBER(s) AFOSR-78-3731
9. PERFORMING ORGANIZATION NAME AND ADDRESS Northeastern University 360 Huntington Avenue Boston, MA 02115		10. PROGRAM ELEMENT, PROJECT, TASK AREA & WORK UNIT NUMBERS 61102F 2311/A1
11. CONTROLLING OFFICE NAME AND ADDRESS AFOSR/NP Building 410 Bolling AFB, DC 20332		12. REPORT DATE 31 Jan 83
		13. NUMBER OF PAGES 99
14. MONITORING AGENCY NAME & ADDRESS(if different from Controlling Office)		15. SECURITY CLASS. (of this report) UNCLASSIFIED
		15a. DECLASSIFICATION/DOWNGRADING SCHEDULE

16. DISTRIBUTION STATEMENT (of this Report)

Released for public release; distribution unlimited

17. DISTRIBUTION STATEMENT (of the abstract entered in Block 20, if different from Report)

18. SUPPLEMENTARY NOTES

19. KEY WORDS (Continue on reverse side if necessary and identify by block number)

20. ABSTRACT (Continue on reverse side if necessary and identify by block number)

A study of a mechanism which can cause the disruption of a stationary electric potential structure was completed. Results were applied to the parrallel electric fields which are associated with auroral arcs. A program of research directed towards analyzing the structure of small scale auroral vortices observed by an Air Force satellite was completed. Two intense auroral events marked by large deflections in the east-west magnetic field component were studied. The events are associated with electric fields whose magnitude can exceed 200 mV/m. Electric field variations give rise to plasma vortex flow patterns similar to these

DD FORM 1 JAN 73 1473 EDITION OF 1 NOV 65 IS OBSOLETE

UNCLASSIFIED

SECURITY CLASSIFICATION OF THIS PAGE (When Data Entered)

observed in auroral folds and curls. Observed values were consistent with collisionless, single-particle theories.

SUMMARY

During this final year we have completed our study of a mechanism which could cause the disruption of steady potential structures associated with auroral arcs. This work resulted in several publications which were collabortive efforts with members of the Department of Plasma Physics, Royal Institute of Technology, Stockholm, Sweden.

We have also completed a study of small scale auroral vortices as observed by Air Force satellite S3-2. This work was a collaborative effort with scientists at AFGL.

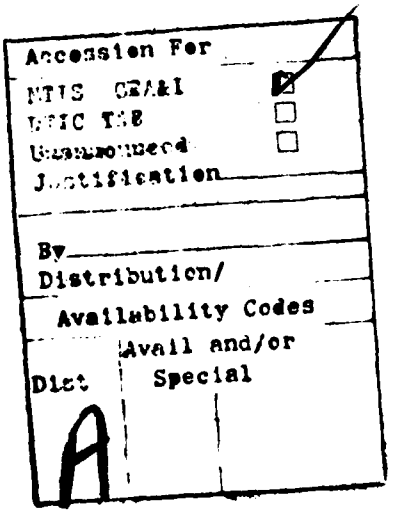

AIR FORCE OFFICE OF SCIENTIFIC RESEARCH (AFSC)
NOTICE OF TRANSMITTAL
This technical report has been reviewed and is
approved for public release IAW AFR 190-12.
Distribution is unlimited.
MATTHEW J. KERPER
Chief, Technical Information Division

I RESEARCH WORK

During the period 1 December 1981 - 31 January 1983 we have completed a study of a mechanism which can cause the disruption of a stationary electric potential structure. Our results were applied to the parallel electric fields which are associated with auroral arcs. These findings were reported in references 1 to 4 listed in section II. Preprints are included in section III. This work was performed in collaboration with several members of the Department of Plasma Physics, Royal Institute of Technology, Stockholm-Sweden.

We have also completed a program of research directed towards analyzing the structure of small scale auroral vortices. These features were observed by the Air Force S3-2 satellite. The work was performed in collaboration with scientists at AFGL. Our results in this area are contained in references 5 and 7.

At this point we shall briefly indicate the directions of future research work which will build on the progress made during the past five years of this grant. First it is intended to further refine our model describing the temporal development of a plasma sheath. This work will focus on the mechanism by which the dynamic Bohm criterion is established at the sheath edge. Prof. C. Birdsall and his group at U. C. Berkely, have expressed an interest in our results and we anticipate that a fruitful collaborative effort will be established in this area. Finally we will continue our work on the dynamic properties of auroral double layers and vortices. It is hoped that our previous results will shed some light on the more global processes that are associated with the breakup phase of a substorm. Our rationale for this hypothesis is the fact that the small scale features that we have focused upon are signatures of this epoch of the storm. In this regard we have submitted a proposal to AFGL to investigate this problem.

At present the study has been approved and funding should commence in February 1983.

Before concluding this section we would like to thank Dr. H. Radoski for his encouragement and support of our research efforts over the period of this grant.

II CUMULATIVE REFERENCES

The works listed in this section were all performed under the auspices of this AFOSR grant. An asterisk (*) beside a listing indicates that the paper is included in section IV of this report.

1.* W.J. Burke, M.B. Silevitch, and D.A. Hardy, Satellite Observations of Small Scale Auroral Vortices, Journal Geophys. Res., accepted for publication (1983).

2.* M.A. Raadu and M.B. Silevitch, On the Negative Resistivity of Double Layers, Submitted to the J. of Plasma Physics, December, 1982.

3.* M.A. Raadu and M.B. Silevitch, Circuit Effects on Pierce Instabilities and Double-Layer Formation, Manuscript Completed, To be Submitted to an Appropriate Journal in January, 1983.

4. Silevitch, M.B., C.G. Falthammar, and L.P. Block, Transient Double Layers as a Source for the 10 Hz Flickering Aurora, presented at the AGU Chapman Conference - Origins of Plasma and Electric Fields in the Magnetosphere, Yosemite, CA, 1982.

5. Silevitch, M.B., Excitation of Transient Double Layers and their Coupling to the Ionosphere, Paper presented at the International Conference on Plasma Physics, Gothenberg, Sweden, June, 1982.

6.* R. Jackson, Second Order Effects Related to a Model for a Parallel Shock, submitted to Journal Geophys. Res., (1982).

7. W.J. Burke, M.B. Silevitch, and D.A. Hardy, Satellite Observations of Small Scale Auroral Vortices, Paper Presented at AGU Fall Meeting, San Francisco, CA, 1982.

8. Raadu, M.A. and M.B. Silevitch, On the Negative Resistivity of Double Layers, Paper presented at the Symposium on Plasma Double Layers, Riso National Laboratory, Roskilde, Denmark, June, 1982.

9. Raadu, M.A. and M.B. Silevitch, On the Role of Pierce Instabilities in Double Layer Formation, presented at the 17th Nordic Symposium on Plasma and Gas Discharges, Geilo, Norway, 1982.

10. E.C. Whipple Jr. and M.B. Silevitch, Ion Current in a Magnetic Neutral Region: Generation of an Incipient Magnetopause, Journal Geophys. Res., 87, 651 (1982).

11. M.E. Greenspan, M.B. Silevitch, and E.C. Whipple, Jr., On the Use of Electron Data to Infer the Structure of Parallel Electric Fields, Journal Geophys, Res. 86, 2175 (1981).

12. M.B. Silevitch, On a Theory of Temporal Fluctuations in the Electrostatic Potential Structures Associated with Auroral Arcs, Journal Geophys. Res. 86, 3573 (1981).

13. J.W. Cipolla and M.B. Silevitch, On the Temporal Development of a Plasma Sheath, Journal of Plasma Physics 25, 373 (1981).

14. R. Jackson, Nonlinear Electrostatic Waves: Oblique Propagation, J. Plasma Phys. 26, 399 (1981).

15. F.T. Berkey, M.B. Silevitch, and N.R. Parsons, Time Sequence Analysis of Flickering Auroras, I. Application of Fourier Analysis, Journal Ceophys. Res. 85, 6827 (1980).

16. E.C. Whipple and M.B. Silevitch, Ion Current in a Magnetic Neutral Line Region, presented at the Fall AGU Meeting, 1980.

17. M.E. Greenspan, M.B. Silevitch, and E.C. Whipple Jr., The Ionosphere as a Source for Mirroring Magnetospheric Electrons, Chapman Conference on Auroral Arcs, Fairbanks, Alaska, 1980.

18. M.B. Silevitch and E.C. Whipple Jr., On Fluctuating Auroral Double Layers, Chapman Conference on Auroral Arcs, Fairbanks, Alaska 1980.

19. M. Greenspan, M. Silevitch, and E. Whipple, Signatures of Parallel Electric Fields in Particle Data, Chapman Conference on High Latitude Electric Fields, Yosemite, CA, 1980, Paper 50.

20. M.B. Silevitch, E.C. Whipple Jr., and M.E. Greenspan, Temporal Behavior of Particle Fluxes Associated with Auroral Arcs, Chapman Conference on High Latitude Electric Fields, Yosemite, CA, 1980, Paper 58.

21. R. Jackson, Parametric Instability Due to Low Frequency Whistler Wave, Phys. Lett. A, 77A, 438, (1980).

22. R. Jackson and K.I. Golden, Formation of Precursor Whistler Mode Plasma Turbulence in Parallel Shock Waves, J. Plasma Phys. 22, 491, (1979).

23. J.W. Cipolla Jr. and M.B. Silevitch, Study of Dynamic Solid Body - Plasma Interaction, American Physical Society Washington meeting April 1979.

24. J.W. Cipolla Jr. and M.B. Silevitch, Analytical Study of the Time Dependent Spacecraft-Plasma Interaction, Spacecraft Charging Technology Conference, Colorado Springs, October 1978.

III PREPRINTS

OBSERVATIONS OF SMALL-SCALE AURORAL VORTICES BY THE S3-2 SATELLITE

William J. Burke, [1]
Michael Silevitch, [2]
David A. Hardy, [1]

ABSTRACT

We have studied two intense auroral events which were encountered by the S3-2 satellite at ~0550 and ~1930 MLT, during a substorm, near the equatorward edge of the region 1 current system. The events are marked by large deflections in the east-west magnetic field component. In the dawn (dusk) event the deflection was 100 (300) nT with a total duration of 4(7) seconds. In both cases the deflection corresponding to an upward current sheet was sharpest, occuring over .25 seconds. Upward current strengths of 45 and 135 μ A/m^2 within latitude extents of < 2 km are inferred. The principal region of return current is not contiguous with the upward current sheet and is more spatially extended, with maximum intensities in the range of 10 to 15 μ A/m^2. The events are associated with electric fields whose magnitude can exceed 200 mV/m. In the region between the current sheets, adjacent to the principal upward current sheet, the electric field rotated by 180° then returned to its original orientation. Such electric field variations give rise to plasma vortex flow patterns similar to these observed in auroral folds and curls. Despite spatial aliasing, the measurements of an electron detector in the vicinity of the upward current sheets provide useful information concerning the density and temperature of the parent populations and the field-aligned potential drop. With some reasonable assumptions, it is shown that observed values of $j_\parallel$ and $\phi_\parallel$ are consistent with collisionless, single-particle theories.

1. Air Force Geophysics Laboratory, Hanscom AFB, MA 01731
2. Electrical Engineering Department, Northeastern U., Boston, MA 02115

Introduction

The purpose of this paper is to present a detailed examination of two small-scale electrodynamic structures observed at low altitudes by the S3-2 satellite. Both events were detected near the dawn-dusk meridian, in the southern auroral ionosphere, during a substorm period. Large-scale features of the substorm period have been simulated by the Rice University group (Harel et al., 1981 a,b; Spiro et al., 1981; Karty et al., 1982; Chen et al., 1982). A preliminary analysis of electric field and field-aligned current measurements during the events has been given by Burke (1981). It was shown that in both instances the satellite passed through paired current sheets. The upward current sheets had latitudinal thicknesses of < 2 km and average current densities, $j_{\parallel}$, of 45 and 135 $\mu A/m^2$. The return (downward) current sheets were latitudinally more extended with $j_{\parallel}$ in the 10 to 15 $\mu A/m^2$ range. Also the principal return current sheets were spatially separated from the intense upward current. In the region between the sheets, but close to the intense upward currents, the electric field underwent rotations then returned to its original orientation. The present analysis considers: (1) $\overline{E} \times \overline{B}$ plasma drift motions in the regions of electric field rotations, and (2) measurements of an electron spectrometer in the vicinity of the current sheets.

Consideration of the $\overline{E} \times \overline{B}$ plasma drift motions reveals the existence of small-scale vortices embedded in regions of large-scale sunward plasma drifts. The vortices are qualitatively similar to auroral curls observed with ground based instrumentation (Hallinan and Davis, (1970). Based on concepts first developed by Alfven (1950) and Webster (1957), Hallinan and Davis (1970) suggested a theoretical model for auroral curl formation where vortices result from shears in the $\overline{E} \times \overline{B}$ drift pattern. This feature is inherent to a partially neutralized auroral charge sheet. Webster and Hallinan (1973) showed that

such structures are unstable so that infinitesimal ripples distorting the drift velocity grow into vortices. The process is analagous to the Kelvin-Helmholtz (K-H) instability of fluid mechanics. Recently Wagner et al. (1981) have demonstrated by a computer simulation, how the electrostatic K-H mechanism leads to the formation of vortices in the auroral charge sheets.

Two essentially different theoretical approaches to the relationship between field-aligned currents ($j_\parallel$) and potential ($\phi_\parallel$). The first approach concerns the transmission of electrical information between magnetospheric generators and ionospheric loads via kinetic Alfven waves (Goertz and Boswell, 1979; Lysak and Carlson, 1981; Lysak and Dum, 1982). The second approach assumes a potential distribution along magnetic field lines and calculates the field-aligned current reaching the ionosphere (Knight, 1973; Lemaire and Scherer, 1973, 1974; Whipple, 1977; Fridman and Lemaire, 1980; Lyons, 1981). The relationship was derived by considering collisionless, single-particle trajectories in a magnetic field. Values of $j_\parallel$ are enhanced by $\Phi_\parallel$ which opens the atmospheric loss cone. The degree to which the loss cone is opened depends on the altitude and the magnitude of $\Phi_\parallel$. The derived relationship between $j_\parallel$ and $\Phi_\parallel$ has been shown to be consistent with rocket measurements of precipitating electron fluxes above an auroral arc (Lyons, 1981). In this paper we compare electron flux measurements with predictions of the second model. Validation of the first model is beyond the capability of S3-2 instrumentation.

The following section provides a brief description of S3-2 instrumentation and a detailed presentation of measurements in the vicinity of the two auroral events. For the sake of coherence, some aspects of the measurements previously reported by Burke (1981) are repeated here. The discussion section focuses on how the observations compare with the theories of auroral curls and $j_\parallel/\Phi_\parallel$ relationships.

Instrumentation

The S3-2 satellite was launched into polar orbit during December 1975 with an initial apogee, perigee and inclination of 1557 km, 240 km and 96.3°, respectively. It is spin-stabilized with a nominal spin period of 20 sec. The spin axis is nearly perpendicular to the orbital plane. The orbital plane itself is subject to a slow westward precession of 1/4° per day. The scientific package on S3-2 includes: (1) an electric field experiment consisting of two dipoles, (2) a triaxial fluxgate magnetometer, and (3) an energetic electron spectrometer. Electric and magnetic field components are usually calculated in a spacecraft centered coordinate system with X positive along the satellite velocity, Z is positive toward local nadir and Y completes the right hand system. When the orbital plane is near the dawn-dusk meridian, as in the cases studied here, Y is positive in the antisunward direction (cf. Figure 1 of Smiddy et al., 1980). In this paper, data are also presented in geomagnetic coordinates.

The instrumentation of S3-2 and the methods used to reduce data have been described in detail by Burke et al. (1980). Briefly, one of the dipoles has a length of 29.72 m. It lies in the satellite's spin plane and measures the electric field component along the satellite trajectory (E_x). The second dipole has a length of 11.18 m and lies close to the satellite's spin axis. As discussed by Mozer et al. (1980), the spin-axis aligned dipole frequently experiences dc offset problems so that only the spin plane data are normally presented. The problems arise from variations in the plasma density and/or chemical composition. The variations in dc offset due to changes in plasma characteristics usually occur on time scales much longer than $\lesssim 10$ sec required for the satellite to traverse the intense electrodynamic shock structures studied below. We have examined simultaneous measurements from two driftmeter experiments on S3-2 (Burke et al., 1980) and have found no evidence of small-scale

variations in the ionospheric plasma characteristics while crossing the structures. In such instances the spin-axis component of the electric field (E_y) can be determined by subtracting dc constar offsets. Potential differences between the ends of the dipole are sampled 32 times per second. To resolve spatio-temporal structures with the highest possible resolution, all of the electric field measurements are used. Magnetic field measurements were taken at a rate of 32 samples per second, with a one bit resolution of 5 nT. All of the data are presented as differences between the measured and IGRF 75 model components. The electron spectrometer measures electrons with energies between 80 eV and 17 KeV in 32 energy channels, compiling a full spectrum every second. The aperture of the instrument is mounted in the spin plane of the satellite. Clearly, the particle-characteristics of structures through which the satellite passes in 0.25 sec cannot be resolved fully with this detector. As seen below, through happy coincidences of energy-sampling and look direction, some useful information about precipitating electrons has been retrieved.

EXPECTED SIGNATURES OF AURORAL VORTICES

Since this paper largely concerns auroral vortices it is useful (before examining the data) to consider their expected signatures in S3-2 measurements. Here and throughout this paper we assume that vortices are time-stationary over the interval of satellite encounter and are reflected in the $\overline{E} \times \overline{B}$ drift motion of ionospheric plasma. This differs somewhat from auroral vortices studied by optical means. Optical signatures reflect the characteristics of energetic, auroral electrons. Such electrons may have more complex drifts than that due to $\overline{E} \times \overline{B}$ motion. Also, if there are field-aligned potential drops the $\overline{E} \times \overline{B}$ drift of energetic electrons and consequent optical vorticity may be larger than the vorticity of cold plasma at S3-2 altitudes.

With these cautions in mind let us consider the situation sketched in Figure 1, which is designed to be representative of the southern hemisphere in

the early morning sector. For simplicity assume that the satellite moves southward with a velocity $\overline{V}_S$ along a magnetic meridian. The magnetic field is directed radially outward from the earth along the -Z axis. The satellite trajectory carries it to the west of a flux tube containing a small, negative space charge. As shown in Figure 1 the electric field due to the negative charge $\overline{E}_C$ is directed radially toward the flux tube. The cold plasma has a counter clockwise rotation $\overline{V}_C = (\overline{E}_C \times \overline{B})/B^2$ around the charged flux tube. The top panel of Figure 1 shows that if the only electric field were due to the space charge, the satellite would measure a field with an X component along the satellite trajectory while the satellite was to the north of the charge. This component would go to zero at the point of closest approach and reverse direction to the south of the charged flux tube. The potential obtained by integrating $\overline{E}_C$ along the satellite trajectory (second panel)

$$\Phi_C = - \int \overline{E}_C \cdot \overline{V}_S \, dt$$

has a minimum value at the point of closest approach. The potential due to a postively charged flux tube would have a maximum at the point of closest approach.

The morning sector of the auroral oval is marked by an equatorward-directed, large-scale convection electric field ($\overline{E}_O$) that has a relatively small westward component. The $\overline{E}_O \times \overline{B}$ drift ($\overline{V}_O$) is mostly in the sunward (eastward) direction. The potential obtained by integrating E_O along the satellite trajectory (third panel of Figure 1)

$$\Phi_O = - \int \overline{E}_O \cdot \overline{V}_S \, dt$$

is a monotoically increasing function.

The trace in the bottom panel of Figure 1 gives the total potential Φ_S measured by the satellite, the superposition of Φ_C and Φ_O. It has a local maximum to the north of the space charge and a local minimum near the point of closest approach. Since cold plasma drifts along equipotential contours,

streamlines of the flow are obtained by connecting equipotential points. The direction of equipotential contours are obtained from the total velocity $\overline{V}_0 + \overline{V}_c$ of the plasma. Note that in the case presented in Figure 1 a vortex in the rest frame of the plasma appears as an S-like reversal of the plasma flow in the satellite frame of reference.

OBSERVATIONS

We now consider the morphology of the two electrodynamic structures. They were detected on opposite sides of the oval during a substorm period on 19 September 1976. In analyzing data we have assumed that S3-2 encountered time-stationary, spatial structures. That is, the time scales for changes in the quasi-dc electric and magnetic fields is long in comparison with the satellite traversal period. Attention was first drawn to these events by their magnetic rather than electric field signatures. Figures 2a and 2b are plots of ΔB_y measured on the dawn and dusk side, southern hemisphere auroral oval passes of Rev 4079A and 4079B, respectively. The data are plotted as functions of UT (in seconds of the day and in hours minutes), invariant latitude, magnetic local time and altitude. The first event begins at 0953:06 UT (Λ = 68°, MLT = 05.4), and appears as a 100 nT excursion of ΔB_y that lasts for 4 seconds. The second event is a 300 nT excursion of ΔB_y beginning at 1148:16 UT (Λ = 67°, MLT = 19.3) and lasting for 7 seconds. The excursions are from a baseline established by the large-scale region 1 and region 2 current system. In both cases the excursions are located near the equatorward edge of the region 1 current sheet. The altitudes of observation were 1050 and 1350 km, respectively. The Birkeland current densities associated with these ΔB_y excursions greatly exceed those normally found near auroral arcs (Choy et al., 1971).

A detailed analysis of the events was performed by examining the individual electric and magnetic field measurements across the events. Rapid fluctuations

(not shown) are found in the potential differences measured across both spinning and axial dipoles. The fluctuations are qualitatively similar to those measured at higher altitudes near small-scale electrostatic "shocks" (Mozer et al., 1977). The satellite was sufficiently high in altitude that variations in the axial dipole measurements across the events were attributed to changing E_y rather than to changing DC offsets on the active elements of the electric field sensors. Values of E_y were calculated by subtracting the electric field component due to satellite motion across magnetic field lines and our best estimate of the DC offset. There may still remain a small, unknown DC bias in the measurements, however, relative variations in E_y are accurate. The electric field components were transformed from satellite to geomagnetic north-south (E_{NS}) and east-west (E_{EW}) coordinates by assuming that $\overline{E} \cdot \overline{B} \approx 0$ everywhere. The three components of $\overline{\Delta B}$ were also computed in geomagnetic coordinates. For the remainder of this section we use the highest possible time resolution for S3-2 measurements of $\overline{E}$ and $\overline{\Delta B}$, considering first the dawn-side then the dusk-side structure.

(i) Dawnside Structure

Figure 3 is a plot of four and one half seconds of electric field measurements in geomagnetic coordinates starting at 35586.2 (0953:06.2) UT. Current densities, derived from the slopes of ΔB_{EW}, are represented in histogram form with positive values corresponding to currents out of the ionosphere. ΔB_{UD} and ΔB_{NS} show no systematic variations across the region of interest. In the quarter of a second after 35586.9 UT ΔB_{EW} increased from 350 to 450 nT. There is a partial recovery in the next eighth of a second followed by a 1.25 second period where ΔB_{EW} shows a very weak slope. This is followed by a pair of current sheets. The principal recovery occurs in approximately 3/4 of a second after this pair of current sheets . The most intense current density is 45 $\mu A/m^2$ directed out of the ionosphere. The return current is more dispersed over

the event. The latitudinal thickness of the upward current sheet projected to an altitude of 100 km is ~ 1.5 km, a typical width of optical arcs when viewed from the ground in the direction of magnetic zenith.

Vector representations in the bottom panel show that the electric field was originally oriented to the west of north and remained that way into the intense current sheet. Between 35586.2 and 35587.0 UT E_{EW} had a nearly constant westward value of ~ 20 mV/m. During the same interval the northward component increased from 50 to 200 mV/m. In the dawnside, southern hemisphere an increasing northward electrostatic field component in satellite coordinates corresponds to a region of negative electric field divergence. Thus, this upward current sheet is also a region of negative space charge. After 35587.2 the electric field rotated through east to southeast then back through east to northwest. It is important to note that E_{EW} and E_{NS} underwent major reversals in a region where $\overline{\Delta B}$ was essentially constant.

Figure 4 is an expanded plot of ΔB_{EW} and E_{NS} (top two traces) in the vicinity of the upward current sheet. The position of the upward current sheet is represented by the shaded area in the bottom panel. The potential Φ (third trace) is obtained by integrating the electric field along the satellite trajectory. The potential has two extrema with $\Phi = 0$ arbitrarily set at the poleward extremum. Every fifth electric field vector in Figure 3 and the equipotential points marked X and O has been used to illustrate the plasma flow velocity V in the fourth panel of Figure 4. Since the $\overline{E} \times \overline{B}$ plasma flow is directed along equipotential surfaces plots of Φ and $\overline{V}$ can be combined to approximate the two dimentional flow characteristics of plasma in the vicinity of the arc (bottom panel). In drawing the flow lines we have endeavored to maintain a divergence free flow pattern in two dimensions since $\overline{\nabla} \cdot (\overline{E} \times \overline{B})$ vanishes in the steady state (if $\overline{J} \cdot \overline{E} = 0$). Comparing the potential distribution in Figure 4 with the bottom panel of Figure 1 we note that the potential maximum at 0953:06.2 UT

lies well above the projection of the potential due to the convection electric field. This suggests that the satellite passed to the east of a postively charged flux tube. The point of closest occurred at 0953:06.2 UT. The satellite than pased to the west of a negatively charged flux tube with closest approach occurring at 0953:06.6 UT. When viewed antiparallel to $\overline{B}$ in the rest frame of the plasma one finds two vortices with clockwise and counterclockwise rotations around the positively and negatively charged flux tubes, respectively. Assuming a radius of ~ 2 km for the counterclockwise vortex we estimate the vorticity ω_s to be ~ 1.2 sec^{-1}. As shown in Figure 4, the counter-clockwise vortex is detached from both the upward auroral current sheet and the adjacent, weak return current sheet.

Since the S3-2 electron spectrometer requires a full second to compile a 32 point energy spectrum care must be exercised interpreting measurements in the vicinity of the spatially narrow current sheet. Figure 5 provides five sequential measurements of directional, differential flux. Dashed lines indicate the one count per sampling interval flux level. To the right of the figure are; (1) the UT at which the spectrum compilation began and, (2) the pitch angle (α) sampled half way through the second. In compiling spectra, energy channels were alternately sampled in increasing then decreasing energy. Energy channels were sampled from high to low energies in the cases of spectra 1, 3 and 5 and from low to high energies in the cases of spectra 2 and 4.

Spectra 1 and 2 show broad thermal distributions typical of diffuse auroral precipitation. Spectrum 3 includes electrons with pitch angles between 108° and 90°. Like spectra 1 and 2, high energy channel measurements were at or near the 1 count level. There is, however, an electron burst with a peak energy of ~ 3 keV that coincides exactly with passage through the intense upward current sheet. As the detector turned toward nadir, (spectra 4 and 5) count rates decreased then vanished. After considering the duskside structure, we return

to discuss the electron burst of spectrum 3 and a similar duskside precipitation event in more detail.

(ii) Duskside Structure

The electric and magnetic field components plotted in Figure 6 show that the duskside structure had the more complex structure. Near the poleward boundary of the structure, E_{NS} decreased from 75 to ~0 mV/m between 42496.8 and 42497.6 UT while E_{EW} maintained a nearly constant, low value. After this time, both components increased in magnitude then reversed directions. The magnitude of E after the reversal exceeded 300 mV/m. The components then returned to their original values. After 42498.0 UT E_{NS} underwent large variations in magnitude, but generally remained southerly in orientation. E_{EW} underwent large variations in both magnitude and direction before returning to a near zero value at 42504.8 UT.

Magnetic field variations across the evening side structure show patterns that on a large scale are similar to those of the morning side structure. In the quarter of a second prior to 42497.8 UT, ΔB_{EW} decreased by 300 nT, corresponding to an average current density over this interval of 135 $\mu A/m^2$. As in the previous case there is a weak return current immediately adjacent to the upward current but the principal recovery in ΔB_{EW} occurs in a region spatially seperated from the upward current. Again, the electric field underwent a rotation, this time of 360° at the equatorward edge of the intense upward current sheet and weak return current sheet pair. The internal structure of the evening side event, however, is much more complex than that of the morning side event. This is reflected in the "multiple current sheets" found between 42497.8 and 49500.8 UT. The intensities of these "current sheets" were calculated from slope of ΔB_{EW} i.e. assuming that the satellite crossed a longitudinally extended structure at normal incidence. The presence of significant variations in ΔB_{NS} as well as ΔB_{EW} indicates that the "multiple current sheet" level of complexity is too simple.

If ΔB_{EW} and ΔB_{NS} varied in the same sense across the structure, then the measurements would indicate that the satellite trajectory crossed a series of current sheets at an angle other than 90°. Indeed similar variations of the two components near the poleward edge of the structure indicate that the arc was crossed at an angle of 9° away from normal incidence. The anticorrelated variations in ΔB_{NS} and ΔB_{EW} near 42500 UT suggest that S3-2 passed close to a line current embedded within an extended sheet current.

A different complexity is found in the measurements taken between 42498.8 and 42499.8 UT. Variations in $\overline{\Delta B}$ coincide with variations in the magnitude, but not direction, of $\overline{E}$. The measurements are consistent with the satellite having detected large amplitude Alfven waves. The relationship between the amplitudes of the electric and magnetic fields of Alfven waves comes directly from Maxwell's equation; $\delta E = V_A \delta B$. The Alfven speed, $V_A = B_o/\sqrt{\mu_o \rho}$, where B_o is the main field of the earth, and ρ the mass of the plasma. In the centered dipole approximation, at an altitude of 1350 km along the $\Lambda = 67°$ field line $B_o = 3.3 \times 10^{-5}$ T. For a dominant ion species of O^+ and a number density between 10^{10} and 10^9 m^{-3}, V_A is between 1.8 and 5.7 x 10^6 m/sec. Thus, for an average variation in δB of 75 nT, as seen in the period of interest, δE should vary between 135 and 420 mV/m. The variation in $\overline{E}$ during this time is ~ 300 mV/m. Ten seconds prior to encountering the structure a planar thermal ion sensor on S3-2 measured a plasma density of 3 x $10^9 m^{-3}$. Note, however, that a linear-regime Alfven wave can not explain the variations in ΔB_{EW} near 42497.8 UT. A 300 nT magnetic field amplitude would require a δE between 540 and 1700 mV/m, far greater than the actually mesured electric field. In the non-linear regime however, Lysak and Dum (1982) have shown that such a simple relationship between ΔB and δE no longer maintains. Finally, we note that even if the variations of E and ΔB between 42498.8 and 42499.8 UT are due to Alfven waves, it is not possible to specify directions

of propagation uniquely. Since E varied in magnitude, but not direction, $\delta \overline{E}$ lies approximately in the NE-SW direction. Unfortunately, establishing an "unperturbed baseline" from which we measure $\delta \overline{B}$ demands an unacceptably high level of subjectivity.

Figure 7 is an expanded plot of the potential (top panel) and flow vectors (bottom panel) in the immediate vicinity of the electric field rotation shown in Figure 6. As in the case shown in Figure 4 the potential has two extrema. In this case, however, the potential maximum lies close to the average convection potential. Even in the satellite frame of reference the flow is dominated by a counterclockwise rotation about a negatively charged flux tube. The point of closest approach occurred at 42497.8 UT. We estimate the radius of the vortex to be 0.75 km and $\omega_s \approx 2.5$ sec^{-1}.

Figure 8 provides six consecutive spectral measurements taken in the vicinity of the duskside event. Odd (even) numbered spectra were sampled from low (high) to high (low) in energies. Poleward of the event (spectrum 1), the electron flux was close to or below instrumental sensitivity. This is also true of the highest energy channels sampled in spectrum 2. Spectrum 2 is marked by a burst of electrons with a peak flux of 8×10^9 e/(cm^2-sec-ster-keV) at 3.5 keV and $\alpha = 151°$. The slopes of the low-energy portions of both spectra 2 and 3 are relatively flat. A peak flux 5×10^9 e/(cm^2-sec-ster-keV) at 1.7 keV was measured in spectrum 3 while the detector was looking close to the direction of the magnetic field. Following the broad thermal distribution of spectrum 4, the flux rapidly decreased to background. Obviously there is a high degree of spatial-temporal aliasing in spectra 2 and 3. However, two purely phenomenological remarks can be made. First, a detailed examination of magnetometer and particle detector data records shows that the 3.5 keV electron burst of spectrum 2 was encountered 1/4 sec prior to (2 km poleward of) the intense upward current sheet. Second,

a flux of 1.2×10^{10} e/(cm^2-sec-ster-keV) for electrons with energies near 80 eV, seen in spectrum 2, is the highest level observed for S3-2's lowest energy channel.

It is possible to glean further, albeit somewhat speculative, information by plotting spectra 3 and 2 of Figures 5 and 8, respectively, as distribution functions, f in Figure 9. The distribution functions of both the morning and evening side electron bursts have peaks at energies of 3.0 and 3.5 keV. Following Burch et al. (1976) we interpret electrons with energies above the peak as accelerated primaries. Those with energies below the peak are interpreted as secondary and degraded, primary electrons. In our semilog plot of f versus energy, the points at and beyond the peak have been fit to straight lines. The burst electrons come from magnetospheric populations that were Maxwellian in energy distribution and accelerated through field-aligned potential drops of 3.0 and 3.5 keV. The slopes of the straight-line fits indicate magnetospheric temperature of ~200 eV. The peak value of the distribution function f_o can be used to estimate the densities of the parent populations. In convenient units,

(1) $\quad f_o(\text{cm}^{-6}\text{-sec}^{-3}) = 8.61 \times 10^{-25} \; n(\text{cm}^{-3})/T^{1.5}(\text{ev})$.

For the morning side f_o was estimated by assuming a potential drop of 3.0 kV and then extrapolating the fit to 3.0 keV. This gives a value of $\sim 9 \times 10^{-29}$ (cm^{-6}-sec^{-3}). For the evening side f_o was estimated by determining the intersection of the linear fit above the peak and the linear fit for the three points below the peak. This gives a value of $\sim 2.8 \times 10^{-28}$ (cm^{-6}-sec^{-3}). Assuming magnetospheric isotropy we estimate the parent densities to be 0.30 cm^{-3} and 0.92 cm^{-3} for the morning and evening side events, respectively. These temperatures indicate that the events occur in the boundary plasma sheet as defined by Winningham et al. (1976). In the evening side event there is also evidence for a higher energy population whose temperature is 4 keV and

density is 1.1 cm^{-3}. For simplicity in later calculations we assume that this population has also been accelerated through a 3.5 kV potential drop. Anticipating The discussion section we compute the quantity

(2) $$j_o = nq\sqrt{kT/2\pi m}$$

for each of these populations. This quantity is the field-aligned current density that would be produced by an isotropic electron distribution in the absence of a field-aligned potential drop. Table 1 gives a compilation of the n, kT, $\Phi_{\parallel}$ and j_o calculated from Figure 9.

TABLE 1

Event	$n(cm^{-3})$	kT(eV)	$\Phi_{\parallel}$ (kV)	j_o ($\mu A/m^2$
Morning (Cold)	0.30	200	3.0	1.2
Evening (Cold)	0.92	200	3.5	3.45
(Hot)	1.1	4000	3.5	18.6

Discussion

In this section we discuss the S3-2 measurements in the light of our present theoretical understanding of (1) the generation of auroral vortices and (2) the relationship between field-aligned currents and potential drops. Although other aspects of the event are of importance, we restrict ourselves in this paper to considering only these two points.

Advances in the technology of low-light-level television cameras and other space-optical systems have allowed the classification of many dynamical auroral features (Oguti, 1981 and references therein). At least three classes of auroral vortices have been identified: spirals, folds and curls. Spirals are large-scale vortices with diameters in the 20 to 1300 km range (Davis and Hallinan, 1976). When viewed antiparallel to the magnetic field B the flow pattern is clockwise. Hallinan (1976) argued that spirals result from a Kelvin-Helmholtz like current sheet instability. Both folds and curls are

small-scale phenomena (Hallinan and Davis, 1970) Folds have wavelengths of between 10 and 50 km; they are characterized by clockwise rotations when viewed antiparallel to $\overline{B}$. Curls have wavelengths between 1 and 9 km and have lifetimes between 0.4 and 2 sec. Their sense of rotation is counterclockwise when viewed antiparallel to $\overline{B}$. Diameters of ~ 2 km are typical of this class of vortices (Webster and Hallinan,1973). It has been proposed that auroral curls are K-H instabilities resulting from a localized excess of electrons within a sheet of precipitating particles (Hallinan and Davis, 1970; Webster and Hallinan, 1973). The two vortex structures encountered by S3-2 most closely resemble auroral curls.

Webster and Hallinan (1973) pointed out that the equations for K-H instabilities driven by either unstable current sheets or unstable charge sheets have the same form. Three aspects of our observations indicate that the vortices reported here do not result from current sheet instabilities. First, as K-H vortices grow, they distort the east-west alignment of the current sheets. The S3-2 vector magnetic field measurements show that the intense current sheets were aligned in the east-west direction. Second, the vortices are detached from rather than embedded in the current sheets. Third, the sense of vorticity in regions where electrons carry unstable currents should be clockwise (cf Table 1 of Webster and Hallinan, 1973) rather than counter-clockwise when viewed antiparallel to $\overline{B}$ as was the case in our observations.

To estimate the vorticity of auroral curls Hallinan and Davis (1970) use the growth rate for K-H instabilities

$$\omega_i = \frac{1}{2} \omega_s \left[(1 - 2ka)^2 - e^{-4ka}\right]^{1/2} \qquad (3)$$

where k is the spatial wave number of the curl system and a is the half-width of the auroral charge sheet. Using observationally derived values $\omega_i = 4.2$ sec^{-1} a = 160 m and ka = 0.15 in equation (3) they calculate a typical vorticity of 28

sec^{-1}. This is in agreement with rocket observations of vorticity ($\omega \sim 20\ sec^{-1}$) near the edge of an arc (Kelley and Carlson, 1977). Recently, Wagner et al. (1981) have performed computer simulations of curl formations that include the effects of partially shielded negative charge sheets. In this case the K-H growth rate is

$$\omega_i = \frac{1}{2}\ \omega_s[(1 - 2\ \Delta ka)^2 - e^{-4ka}]^{1/2} \tag{4}$$

Equation (4) reduces to the unshielded case, represented by equation (3) when the parameters $\Delta = 1$. Their simulations show that for increased shielding (decreasing Δ) the maximum growth occurs at increased values of ka but the ratio ω_i / ω_s decreases.

Several points of comparison should be made. First, vortices typical of auroral curls calculated by Hallinan and Davis greatly exceed those estimated from S3-2 measurements of the auroral electric field but not those found in rocket measurements. It should be noted, however, that the auroral sheet thicknesses of 160 m used by Hallinan and Davis in their calculations of ω_s could not be resolved at sampling rates used by S3-2. To resolve a plasma vortex at least two electric fields samples are required. For S3-2 this requires 1/16 sec, or a vortex diameter of 500 m. The vortices detected by S3-2 had radii of 2 km and 0.75 km. If Hallinan and Davis had used a vortex radius of 1 km, an average curl wavelength of 5 km and a growth rate of 4.2 sec^{-1}, then the vorticity determined from equation (3) is 5.6 sec^{-1}. This is much closer to our estimated vorticities of 1.2 and 2.5 sec^{-1}. Second, in the simulations of Wagner et al. (1981) and in the rocket measurements the curls are embedded in the unstable charge sheet. We have already pointed out that the vorticies are detached from the current sheets which may account for the lower vorticity. Because the particle detector was sampling low energy channels as S3-2 passed through the vortices, it is not clear whether a ground-based television camera would have detected the vortices inside a visible auroral arc.

Another point of interest is that both the rocket and the satellite data indicate large-scale electric fields in the range of 100 mV/m. This is considerably less than the estimate of 500 mV/m in the vicinity of auroral curls made by Halliman and Davis (1970). The most likely explanation is that the apparent motion of the curls is due to the large perpendicular electric fields near the source of auroral beams at $\approx 1R_e$ (Mozer et al., 1977) which attenuate in mapping to ionospheric altitudes.

Finally, it is worth reiterating the point made by Kelley and Carlson (1977) that vortices at the edge of auroral arcs may create some portion of the observed high-latitude irregularities in plasma density. Since it is likely that horizontal gradients in plasma density exist near auroral arcs, the perturbed velocity field will create density fluctuations via the term

$$\partial n / \partial t = V \cdot \bar{\nabla} n$$

If vortices with $V \approx 500$ m/s operate on a 10 km density gradient, the irregularity growth rate is .05 sec^{-1} which is higher than many proposed plasma instabilities.

In the introduction of this paper, we noted that several investigators have studied relationships between $j_\parallel$ and $\Phi_\parallel$. A field-aligned potential drop opens the atmospheric loss cone for individual particles in ways that depend on the location in altitude of $\Phi_\parallel$. Assuming an isotropic, Maxwellian parent population, Lyons (1981) has shown that the field-aligned current density is

$$(5) \qquad j_\parallel = j_o \frac{B_i}{B_v} \left[1-(1-\frac{B_v}{B_i}) \exp\left\{ - \frac{e \Phi_\parallel}{kT(\frac{B_i}{B_v} -1)} \right\} \right]$$

where j_o is defined in equation (2); B_i and B_v are the magnetic field strengths at the ionsphere and at the top of the voltage drop, respectively. Information about the altitude of the potential drop is contained in the B_i/B_v ratio. In the limit $B_i/B_v = 1$, the potential drop is located just above the ionosphere, and $j_\parallel = j_o$ no matter how large the potential drop. In the limit $q \Phi_\parallel / kT \to \infty$,

$j_\parallel = j_o B_i/B_o$. Figure 10 is a plot of $j_\parallel/j_o$ versus $q\,\Phi_\parallel/kT$ for six values of B_i/B_v.

Crossing the morning event the S3-2 magnetometer measured an upward current density of 45 $\mu A/m^2$. The values of j_o and $q\,\Phi_\parallel/kT$ inferred from the particle detector measurements are 1.2 $\mu A/m^2$ and 15, respectively. This event designated by the letter M in Figure 10, lies well above all of the current-voltage characteristic curves.

In the evening sector event we measured two populations, one hot (kT = 4 keV) and one cold (kT = 200 eV). We now attempt to evaluate their relative contributions to $j_\parallel$. Magnetometer data presented in Figure 4 shows that $j_\parallel = 135\ \mu A/m^2$. The values of j_o for the hot and cold electrons are 18.6 and 3.45 $\mu A/m^2$, respectively; $\Phi_\parallel = 3.5$ kV. Using the symbols H and C in Figure 9 we have marked the current-voltage relationship one gets by assuming that either the hot (H) or the cold (C) electrons is solely responsible for $j_\parallel$. Both points are well above the theoretical curves. Thus, if the theoretical relationships between $j_\parallel$ and $\Phi_\parallel$ are valid then the current cannot be carried by just one of the populations.

We next assume that the hot population carries the current prescribed by the $j_\parallel/\Phi_\parallel$ relationship. For $q\,\Phi_\parallel/kT = 0.875$, $j_\parallel \approx 1.7\ j_o \approx 32\ \mu A/m^2$. Thus, the cold population must be responsible for 103 $\mu A/m^2$. This is plotted as point C' in Figure 10. Point C' also lies well above any characteristic curve. Similarly if we assume that the cold population carries the current prescribed by the $j_\parallel/\Phi_\parallel$ relationship, we find that the hot population (point H' in Figure 10) must carry almost twice the predicted current.

In order to reconcile S3-2 measurements with theoretical predictions it is necessary to assume that we have underestimated either $\Phi_\parallel$ or n in analyzing the electron measurements. For example, if $\Phi_\parallel$ has a latitudinal gradient, a common feature of inverted-V precipitation, then our estimate of $\Phi_\parallel$ would only be a

lower bound. This provides a viable explanation of the evening side event. Recall that the evening side electron burst was detected 0.25 sec prior to (2 km poleward of) the intense current sheet. We find that if $\phi_{\parallel}$ rose to 5.1 kV above the arc then the observations and theory agree. The points plotted as H" and C" show that with $\phi_{\parallel}$ = 5.1kV the hot population carries a current of 45 μ A/m^2 and the cold population carries 100 μ A/m^2.

The morning side electron burst exactly coincides with the 45 μ A/m^2 upward current sheet. Thus, a gradient in $\phi_{\parallel}$ is not a likely explanation of discrepancies between observations and theory. However an underestimate of the parent density is a possible explanation. Recall that the morning-side, burst electrons were detected while the detector was sampling pitch angles near 90°. Burch et al. (1979) have found that, at least in the case of polar cap acceleration events, the highest levels for electrons in the peak channel are found along the direction of the magnetic field. Thus, using a value f_0 measured near 90° pitch angles (Eq.(1)) to calculate n could lead to a serious underestimate. Agreement with theory requires that the parent density be 0.75 cm^{-3} rather than our estimated value of 0.3 cm^{-3}. In both the morning and evening events, the theory and measurements agree only if the ratio B_i/B_v is relatively high. This suggests that for high values of $j_{\parallel}$ the field-aligned potential drop must begin at high altitudes.

One final comment is appropriate. Lyons (1981) stresses the fact that collisionless, single particle theory takes us along way toward understanding the $j_{\parallel} / \phi_{\parallel}$ relationship. Conversely, theories of anomalous resistivity, such as that proposed by Kindel and Kennel (1971) have little applicability for auroral currents. In the case of upward curents, this may be both true and beside the point. The model of Kindel and Kennel concerns plasmas whose ions and electrons have a relative drift motion along B, not a beam of energetic electrons passing through a stationary ionospheric plasma. The model does apply to auroral

return currents which are mostly carried by upwelling, cold electrons. Burke et al. (1980) studied the case of a 10 $\mu A/m^2$ return current from a discrete arc. In this case the measured plasma parameters satisfied Kindel and Kennell criteria for marginal stability. Within this downward current sheet, S3-2 detected an electric field component also directed along B into the ionosphere. It is of interest that in the cases presented here currents out of the ionosphere were 45 and 135 $\mu A/m^2$ while those directed into the ionosphere were restricted to 10 to 15 $\mu A/m^2$ range. The latter numbers require cold plasma drifts near Kindel and Kennel limit of stability.

Summary and Conclusions

In this paper we have presented a detailed analysis of two unusual auroral events observed by S3-2. Both events were characterized by: (1) upward current sheets with latitudinal thicknesses of < 2 km and field-aligned current densities greatly in excess of a few $\mu A/m^2$, (2) return currents with maximum intensities in the 10 to 15 $\mu A/m^2$ range, with the principal return spatially separated for the upward current, (3) electric field rotations driving plasma vortices at locations slightly detached from the upward current sheets, and (4) bursts of electrons accelerated through potential drops of several kilovolts.

The counterclockwise vortices observed by S3-2 have characteristics similar to auroral curls. The results are consistent with theoretical and computer models that indicate that the vortices result form unstable, auroral charge sheets.

At first view the $j_\parallel / \Phi_\parallel$ measurements do not appear to agree with the predictions of collisionless, single-particle theory. We note, however, that if: (1) $\Phi_\parallel$ had a maximum value of 5.1 kV above the evening-side, upward current sheet, and (2) the density of the morning side event's parent population has been underestimated, then agreement between theory and observations is possible. In both instances the field-aligned potential must extend to relatively great altitudes above the auroral ionosphere.

ACKNOWLEDGEMENTS

We wish to thank R. Bostrom of the Uppsala Ionospheric Observatory, C.-G. Falthammer of Royal Institute of Technology, Stockholm and M.C. Kelley of Cornell University for helpful discussions and comments on the text. This work was supported in part under AFOSR contract 78-3731 with Northeastern University.

References

Alfven, H., Cosmical Electrodynamics, Oxford University Press, Oxford, p. 206, 1950.

Burch, J.L., S.A. Fields, W.B. Hanson, R.A. Heelis, R.A. Hoffman and R.W. Janetzke, Characteristics of auroral electron acceleration regions observed by Atmosphere Explorer C, J. Geophys. Res., 81, 2223, 1976.

Burch, J.L., S.A. Fields, R.A. Heelis, Polar cap electron acceleration regions, J. Geophys. Res., 84, 5863, 1979.

Burke, W.J., Electric Fields, Birkeland currents and electron precipitation in the vicinity of discrete auroral arcs, in Physics of Auroral Arc Formation, ed. by S.-I. Akasofu, and J.R. Kan, American Geophysical Union, Geophysical Monograph 25, Washington, D.C., p. 164, 1981.

Burke, W.J., D.A. Hardy, F.J. Rich, M.C. Kelley, M. Smiddy, B. Shuman, R.C. Sagalyn, R.P. Vancour, P.J.L. Wildman and S.T. Lai, Electrodynamci structure of the late evening sector of the auroral zone, J. Geophys. Res., 85, 1179, 1980.

Chen, C.-K., R.A. Wolf, M. Harel, J.L. Karty, Theoretical magnetograms based on quantitative simulation of a magnetospheric substorm, submitted to J. Geophys. Res., 1982.

Choy, L.W., R.L. Arnoldy, W. Potter, P. Kintner and L.J. Cahill, Jr., Field-aligned currents near an auroral arc, J. Geophys. Res., 76, 8279, 1971.

Davis, T.N., and T.J. Hallinan, Auroral spirals 1. observations, J. Geophys. Res., 81, 3953, 1976.

Friden, M., and J. Lemaire, Relationship between auroral electron fluxes and field-aligned electric potential difference, J. Geophys. Res., 85, 664, 1980.

Goertz, C. K. and R.W. Boswell, Magnetosphere-ionosphere coupling, J. Geophys. Res., 84: 7239, 1979.

Hallinan, T.J., Auroral spirals 2. theory, J. Geophys. Res., 81, 3959, 1976.

Hallinan, T.J., and T.N. Davis, Small-scale auroral arc distortions, Planet Space Sci, 18, 1735, 1970.

Harel, M., R.A. Wolf, P.H. Reiff, R.W. Spiro, W.J. Burke, F.J. Rich, and M. Smiddy, Quantitative simulation of a magnetospheric substorm, 1. model logic and overview, J. Geophys. Res., 86, 2217, 1981a.

Harel, M., R.A. Wolf, R.W. Spiro, P.H. Reiff, C-K. Chen, W.J. Burke, F.J. Rich and M. Smiddy, Quantitative simulation of a magnetospheric substorm, 2. comparison with observations, J. Geophys. Res., 86, 2242, 1981b.

Karty, J.L., C.-K. Chen, R.A. Wolf, M. Harel, and R.W. Spiro, Modeling of high-latitude currents in a substorm, J. Geophys. Res., 87, 777, 1982.

Kelley, M.C., and C.W. Carlson, Observations of intense velocity shear and associated electrostatic waves near an auroral arc, J. Geophys. Res., 82, 2343, 1977.

Kindel, J.M., and C.F. Kennell, Topside current instabilities, J. Geophys. Res., 76, 3065, 1971

Knight, L., Parallel electric fields, Planet. Space Sci., 21, 741, 1973.

Lemaire, J. and M. Scherer, Plasma sheet particle precipitation: a kinetic model, Planet. Space Sci., 21, 281, 1973.

Lemaire, J. and M. Scherer, Ionosphere-plasmasheet field-aligned currents and parallel electric fields, Planet. Space Sci., 22, 1485, 1974.

Lyons, L.R., The field-aligned current versus electric potential relation and auroral electrodynamics, in Physics of Auroral Arc Formation, ed. by S.-I. Akasofu and J.R. Kan, American Geophysical Union, Geophysical Monograph 25, Washington D.C., p. 252, 1981.

Lysak, R.L. and C.W. Carlson, The effect of microscopic turbulence on magnetosphere ionosphere coupling, Geophys. Res. Lett., 8: 269, 1981.

Lysak, R.L. and C.T. Dum, Dynamics of magnetosphere-ionosphere coupling including turbulent transport, J. Geophys. Res., (accepted for publication, 1982).

Mozer, F.S., C.W. Carlson, M.K. Hudson, R.B. Torbert, B. Parady, J. Yatteau, and M.C. Kelley, Observations of paired electrostatic shocks in the polar magnetosphere, Phys. Res. Lett., 38, 292, 1977.

Mozer, F.S., C.A. Cattell, M.K. Hudson, R.L. Lysak, M. Temerin and R.B. Torbert, Satellite measurement and theories of low altitude auroral particle acceleration, Sp. Sci. Rev., 27, 155, 1980.

Oguti, T., TV observations of auroral arcs, in Physics of Auroral Arc Formation, ed by S.-I. Akasofu and J.R. Kan, American Geophysics Union, Monnograph 25, Washington, D.C. p.31, 1981.

Smiddy, M., W.J. Burke, M.C. Kelley, N.A. Saflekos, M.S. Gussenhoven, D.A. Hardy and F.J. Rich, Effects of high latitude conductivity on observed convection electric fields and Birkeland currents, J. Geophys. Res., 85, 6811, 1980.

Spiro, R.W., M. Harel, R.A. Wolf, and P.H. Reiff, Quantitative simulation of magnetospheric substorm, 3. plasmaspheric electric fields and evolution of plasmapause, J. Geophys. Res., 86, 2261, 1981.

Wagner, J.S., J.R. Kan, S.-I. Akasofu, T. Tajima, J.N. Leboeuf and J.M. Dawson, A simulation study of V-potential double layers and auroral arc deformations, in Physics of Auroral Arc Formation, ed. by S.-I. Akasofu and J.R. Kan, American Geophysical Union, Geophysical Monograph 25 Washington, D.C., p. 304, 1981.

Webster, H.F. Structure in magnetically confinded electron beams, J. Appl. Phys., 28, 1395, 1957.

Webster, H.F., and T.J. Hallinan, Instabilities in charge sheets and current sheets and their possible occurrence in the aurora, Radio Science, 8, 475, 1973.

Whipple, E.C., The signature of parallel electric fields in a collisionless plasma, J. Geophys. Res., 82, 1525, 1977.

Winningham, J.D., F. Yasuhara, S.-I. Akasofu and W.J. Heikkila, The latitudinal morphology of 10-eV to 10-keV electron fluxes during magnetically quiet and disturbed times in the 2100-0300 MLT sector, J. Geophys. Res., 80, 3148, 1975.

Figure Captions

Figure 1. Sketch of satellite pass to west of a negatively charged flux tube. The electric fields and $\overline{E} \times \overline{B}$ drifts due to the space charge electric field $\overline{E}_c$ and the main, convection electric field $\overline{E}_0$ are indidicated, the panels give the x component of E_c measured by the satellite. The potentials due to the space charge Φ_c, convection Φ_0 and their superposition Φ_s as functions of time (distance) along the satellite trajectory.

Figure 2. Measurements of ΔB_y for S3-2 passes over the dawn-side, southern hemisphere, auroral oval during Rev. 4079A/S, (top) and Rev 4079 B/S (bottom). Rough estimates of region 1, region 2 and polar cap positions are provided for reference.

Figure 3. The up-down (UD), north-south (NS) and east-west components of $\overline{\Delta B}$ in geomagnetic coordinates across dawn-side event. Values of $j_\parallel$ are positive for currents out of the ionosphere. Vector representations of the electric field components are also in geomagnetic coordinates.

Figure 4. Expanded plot of morning side event. The top three plots give the east-west magnetic deflection, the north-south electric field component and the potential along the satellite trajectory. The next panel gives the $\overline{E} \times \overline{B}$ drift velocity $\overline{V}$. The bottom panel combines the Φ and $\overline{V}$ plots to approximate the two dimensional plasma flow in the vicinity of the upward current sheet.

Figure 5. Five consecutive directional differential flux spectra observed near the morning-side event. The UT's at which spectra accumulations began as well as the pitch angles sampled half way through the one second accumulation periods are provided. Dashed lines give the one count per accumulation-period sensitivity of the detector.

Figure 6. Magnetic field deflections, current intensities and electric field vectors for evening-side structure in the same format as Figure 3.

Figure 7. Expanded plot of the potential and flow pattern in the vicinity of the evening-side upward current sheet.

Figure 8. Six consecutive spectra measured near evening side event in the same format as Figure 5.

Figure 9. Semilog plot of distribution function versus energy for spectrum 3 of Figure 5 (top panel) and spectrum 2 of Figure 8 (botton panel). Dashed lines indicate the one count per accumulation period sensitivity of the dectector.

Figure 10. Plot of $j_{\parallel}/j_o$ versus $kT/\phi_{\parallel}$ for various B_v/B_j ratios.

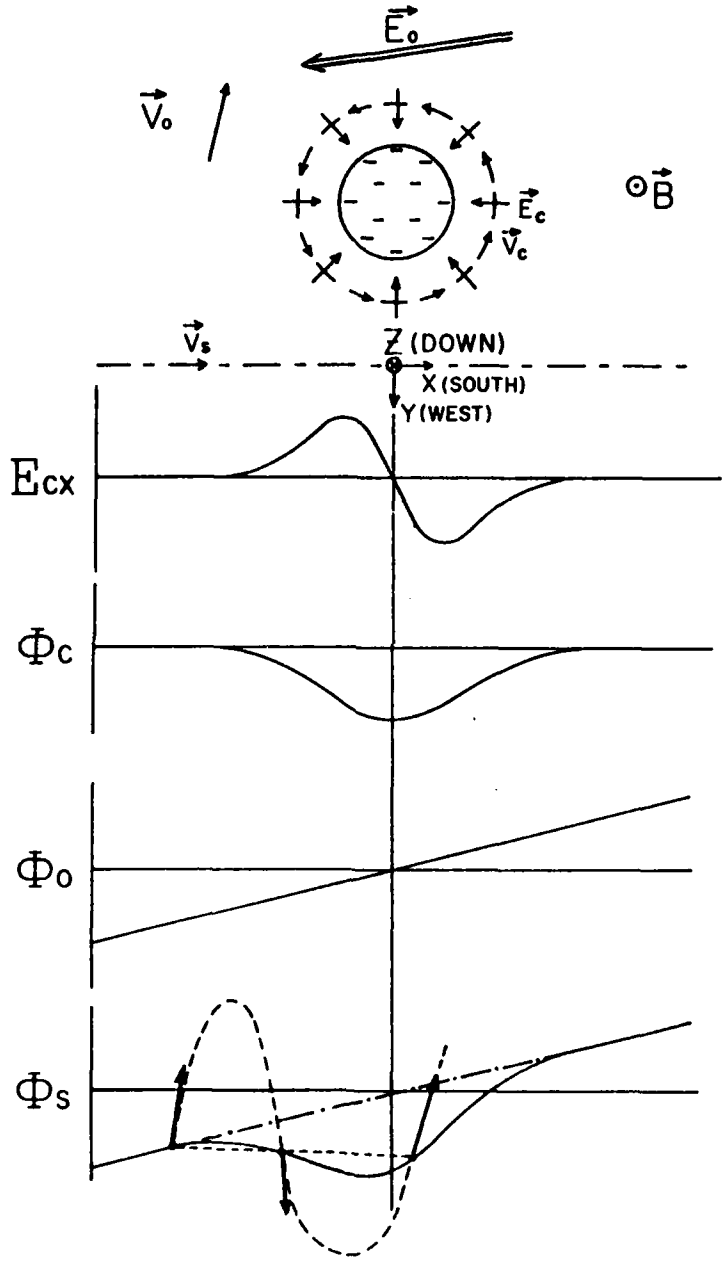
$\vec{E}_o$
$\vec{V}_o$
$\vec{E}_c$
$\vec{V}_c$
$\odot\vec{B}$
$\vec{V}_s$
Z (DOWN)
X (SOUTH)
Y (WEST)
E_{cx}
Φ_c
Φ_o
Φ_s

Figure 1

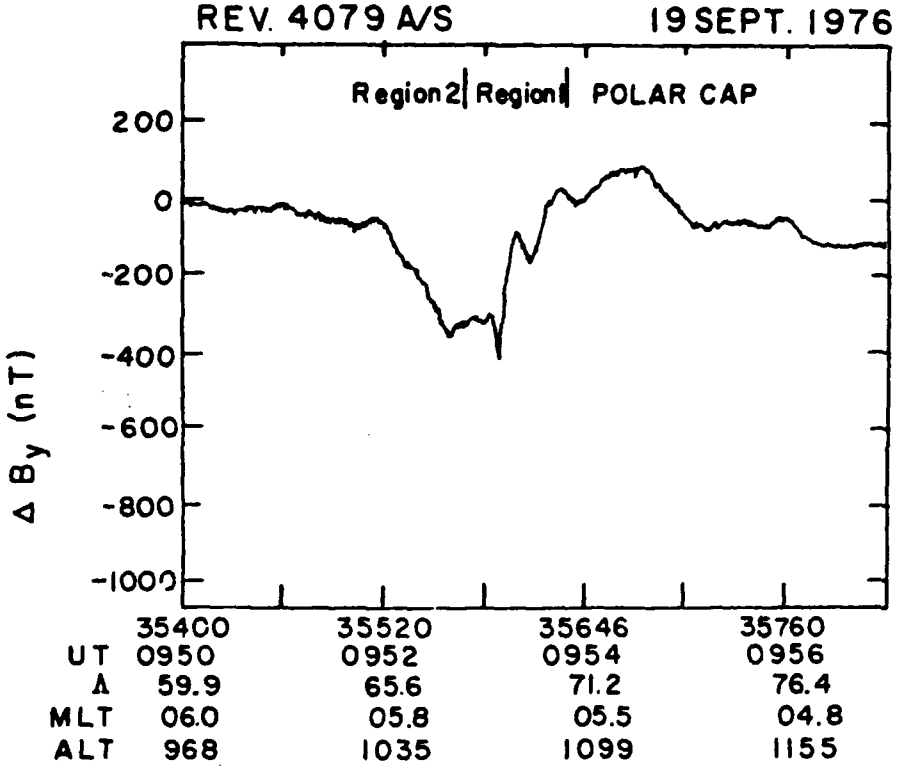
REV. 4079 A/S
19 SEPT. 1976
Region 2
Region 1
POLAR CAP
200
0
-200
-400
-600
-800
-1000
Δ By (nT)
35400
35520
35646
35760
UT 0950
0952
0954
0956
Λ 59.9
65.6
71.2
76.4
MLT 06.0
05.8
05.5
04.8
ALT 968
1035
1099
1155

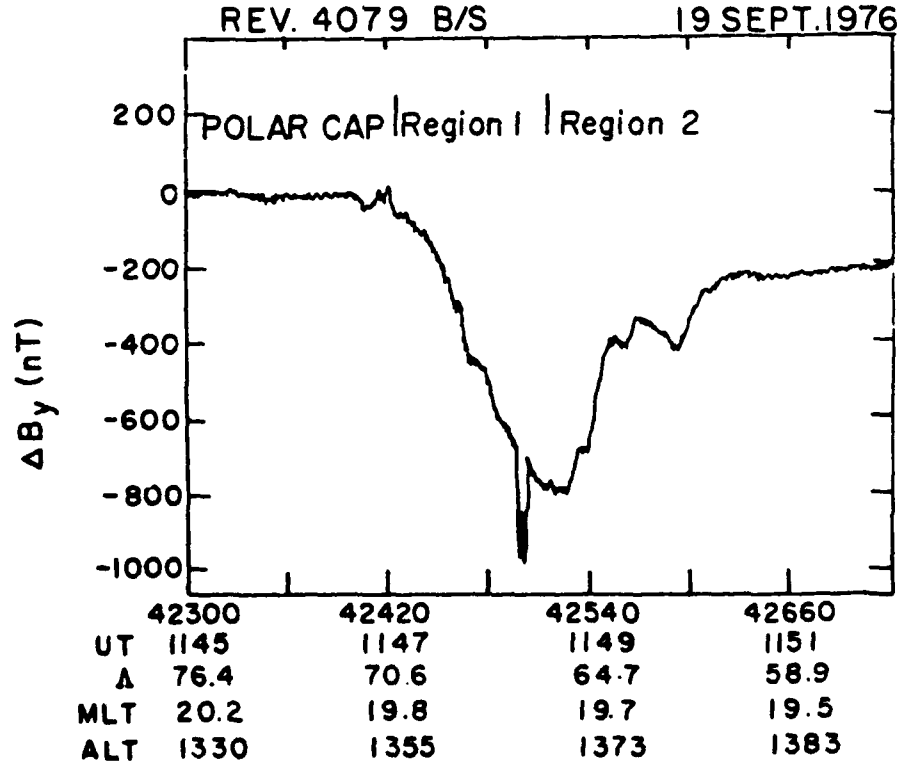
REV. 4079 B/S
19 SEPT. 1976
POLAR CAP
Region 1
Region 2
200
0
-200
-400
-600
-800
-1000
ΔBy (nT)
42300
42420
42540
42660
UT 1145
1147
1149
1151
Λ 76.4
70.6
64.7
58.9
MLT 20.2
19.8
19.7
19.5
ALT 1330
1355
1373
1383

Figure 2

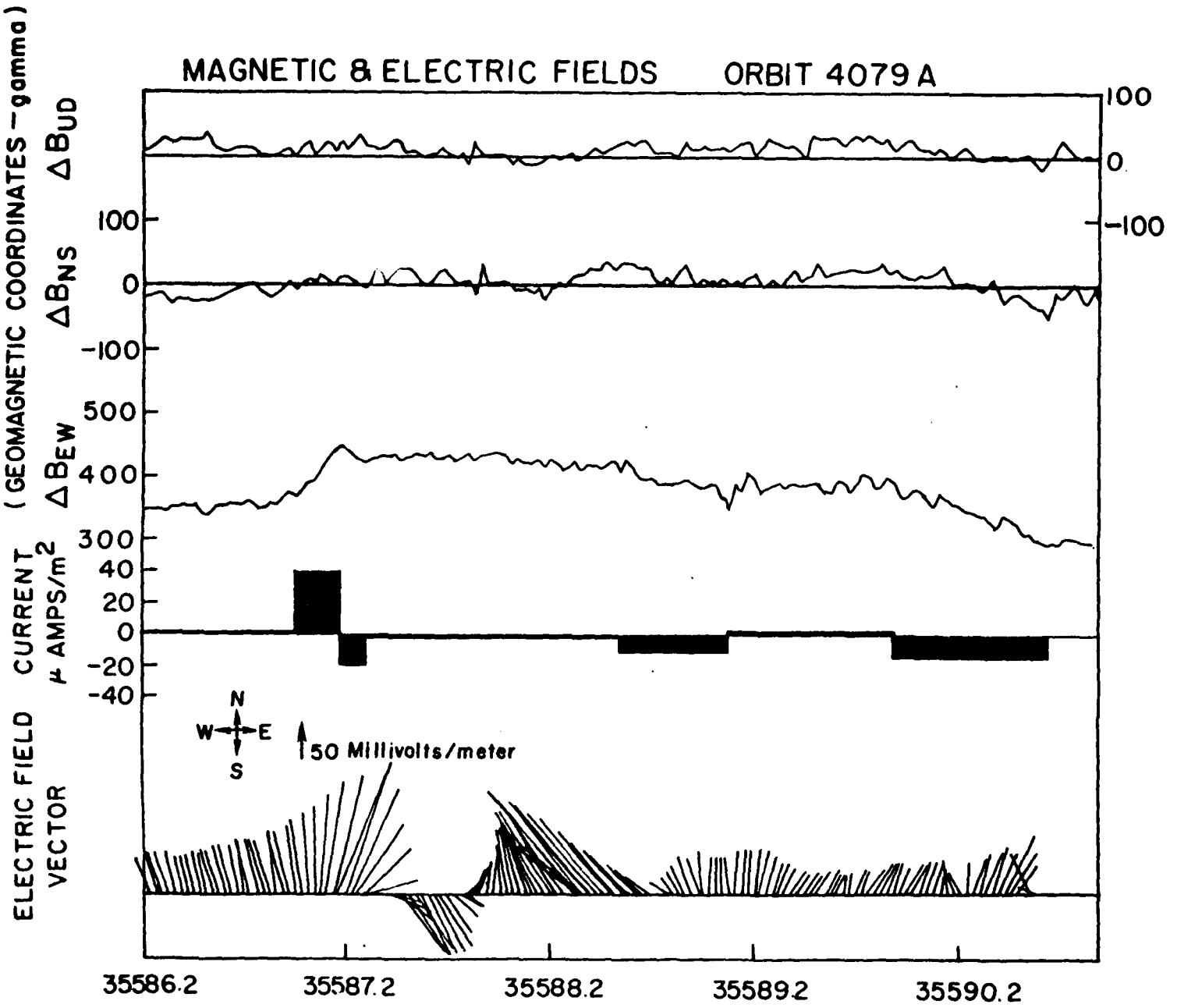
MAGNETIC & ELECTRIC FIELDS ORBIT 4079 A
(GEOMAGNETIC COORDINATES - gamma)
ΔBUD
ΔBNS
ΔBEW
100
0
-100
500
400
300
CURRENT μ AMPS/m2
40
20
0
-20
-40
N
W
E
S
50 Millivolts/meter
ELECTRIC FIELD VECTOR
35586.2
35587.2
35588.2
35589.2
35590.2

Figure 3

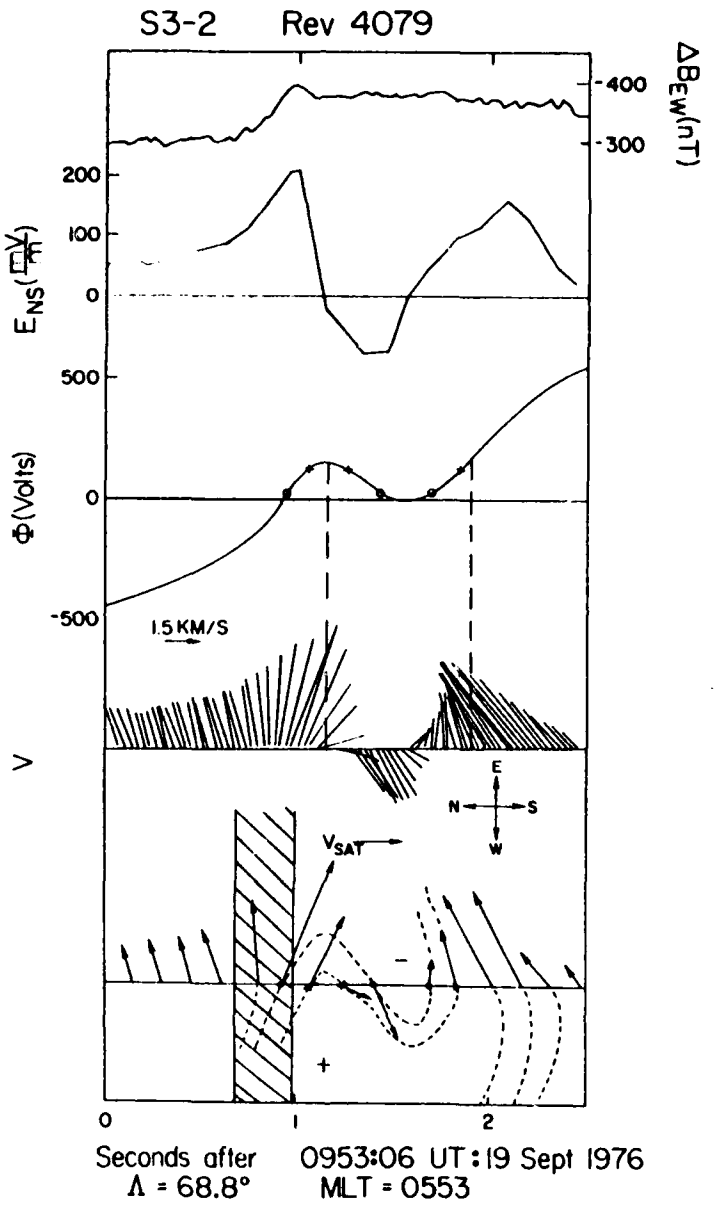
S3-2 Rev 4079
ΔBEW(nT)
-400
-300
200
100
0
500
0
-500
ENS(mV/m)
Φ(Volts)
1.5 KM/S
V
E
N
S
W
VSAT
-
+
0
1
2
Seconds after 0953:06 UT: 19 Sept 1976
Λ = 68.8° MLT = 0553

Figure 4

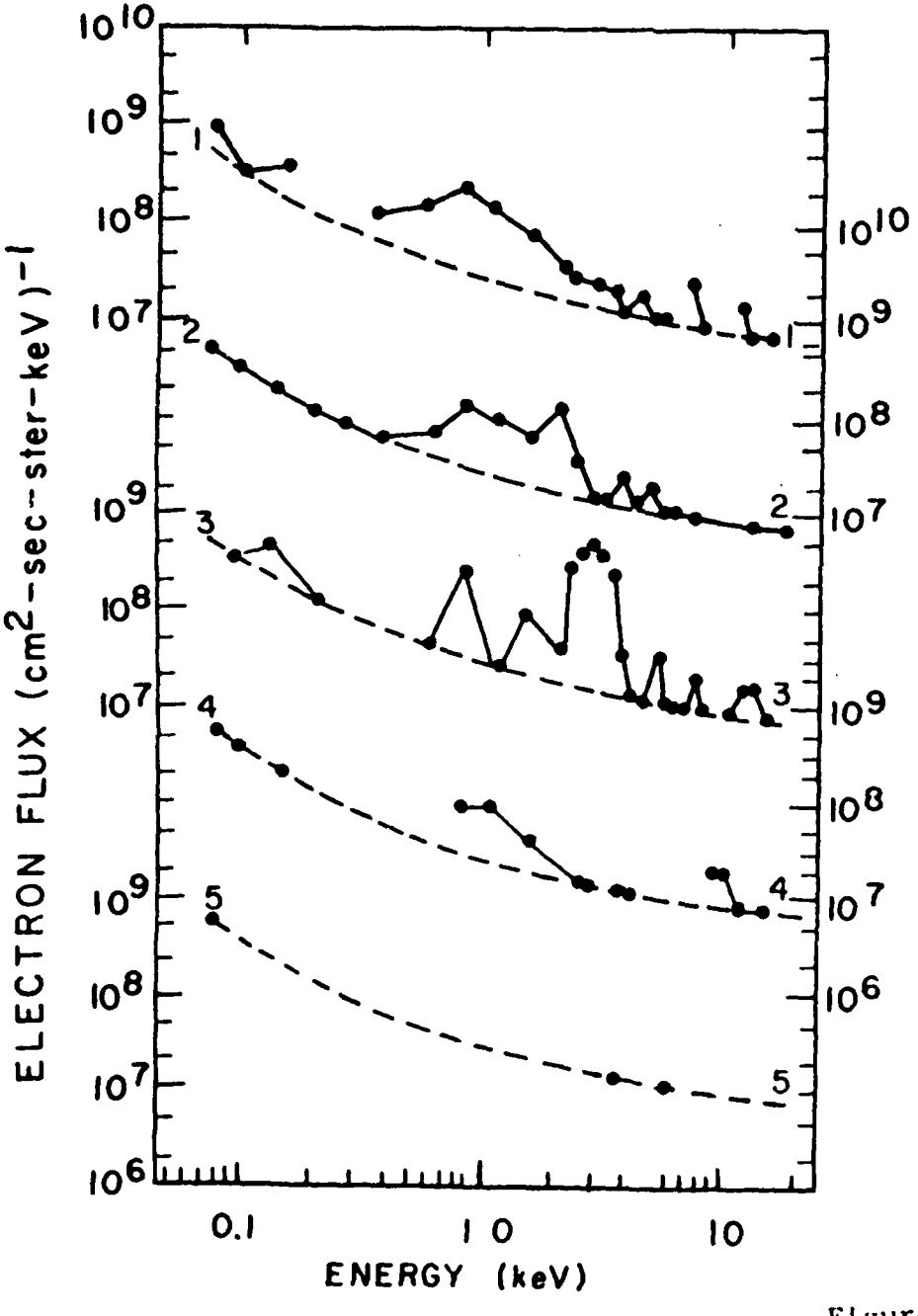

	UT	PITCH ANGLE
1	35584.6	138°
2	35585.6	119°
3	35586 6	99°
4	35587.6	79°
5	35588.6	60°

Figure 5

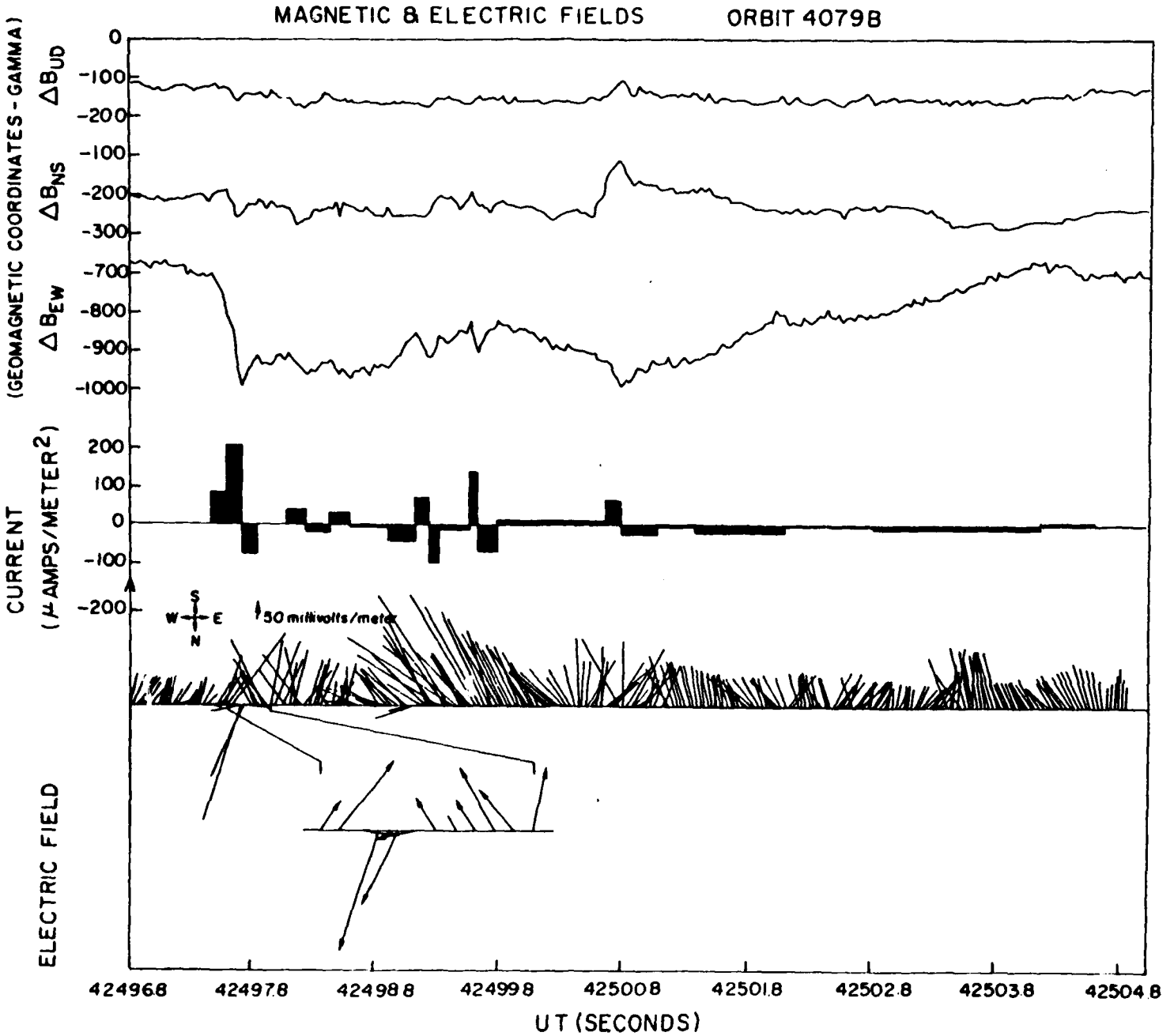
MAGNETIC & ELECTRIC FIELDS
ORBIT 4079B
(GEOMAGNETIC COORDINATES - GAMMA)
ΔB_{UD}
ΔB_{NS}
ΔB_{EW}
0
-100
-200
-100
-200
-300
-700
-800
-900
-1000
CURRENT
(μAMPS/METER^2)
200
100
0
-100
-200
S
W
E
N
50 millivolts/meter
ELECTRIC FIELD
424968
424978
424988
424998
425008
425018
425028
425038
425048
UT (SECONDS)

Figure 6

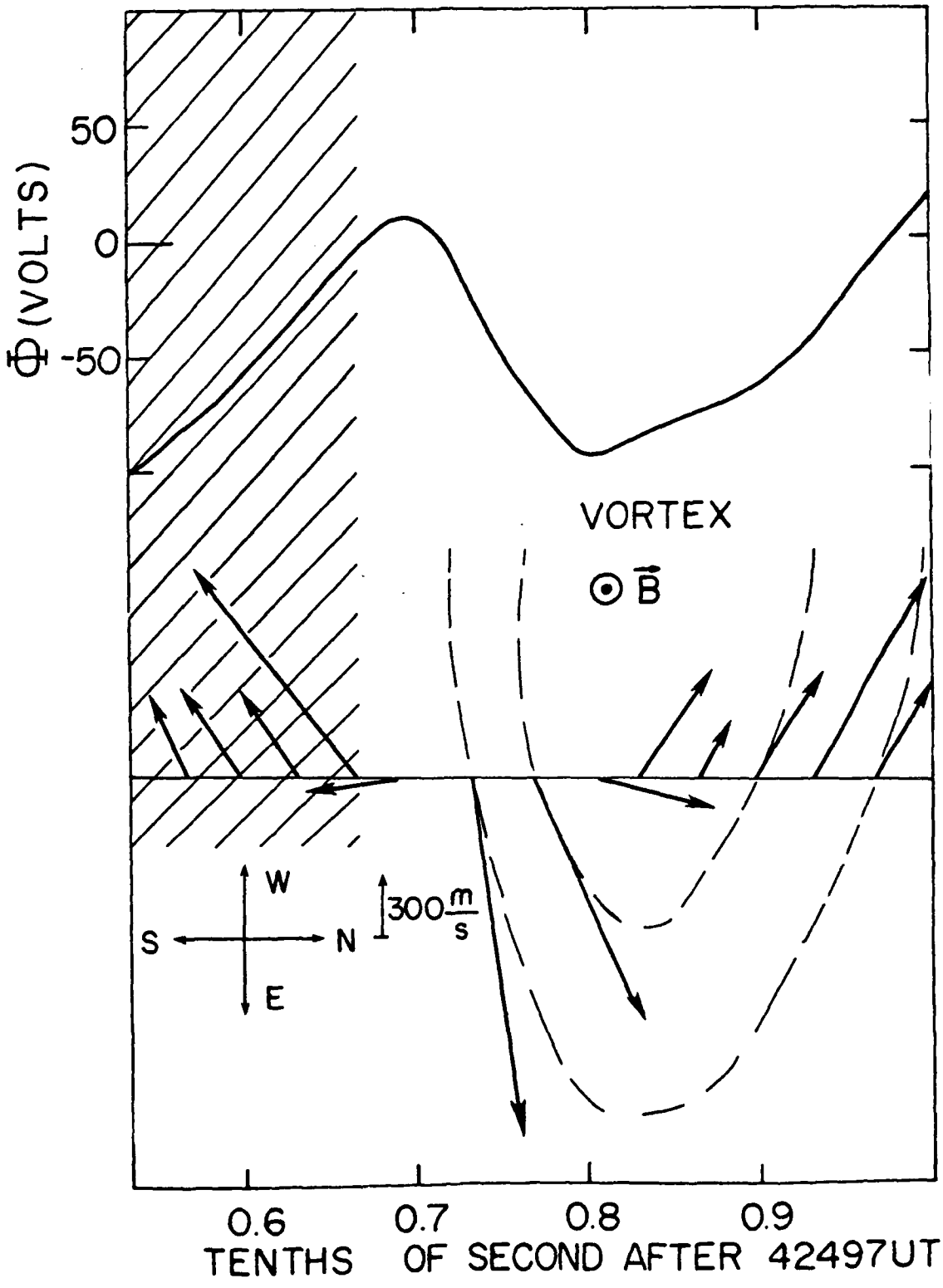
50
0
-50
Φ (VOLTS)
VORTEX
⊙ B
W
S
N
E
300 m/s
0.6
0.7
0.8
0.9
TENTHS OF SECOND AFTER 42497UT

FIGURE 7

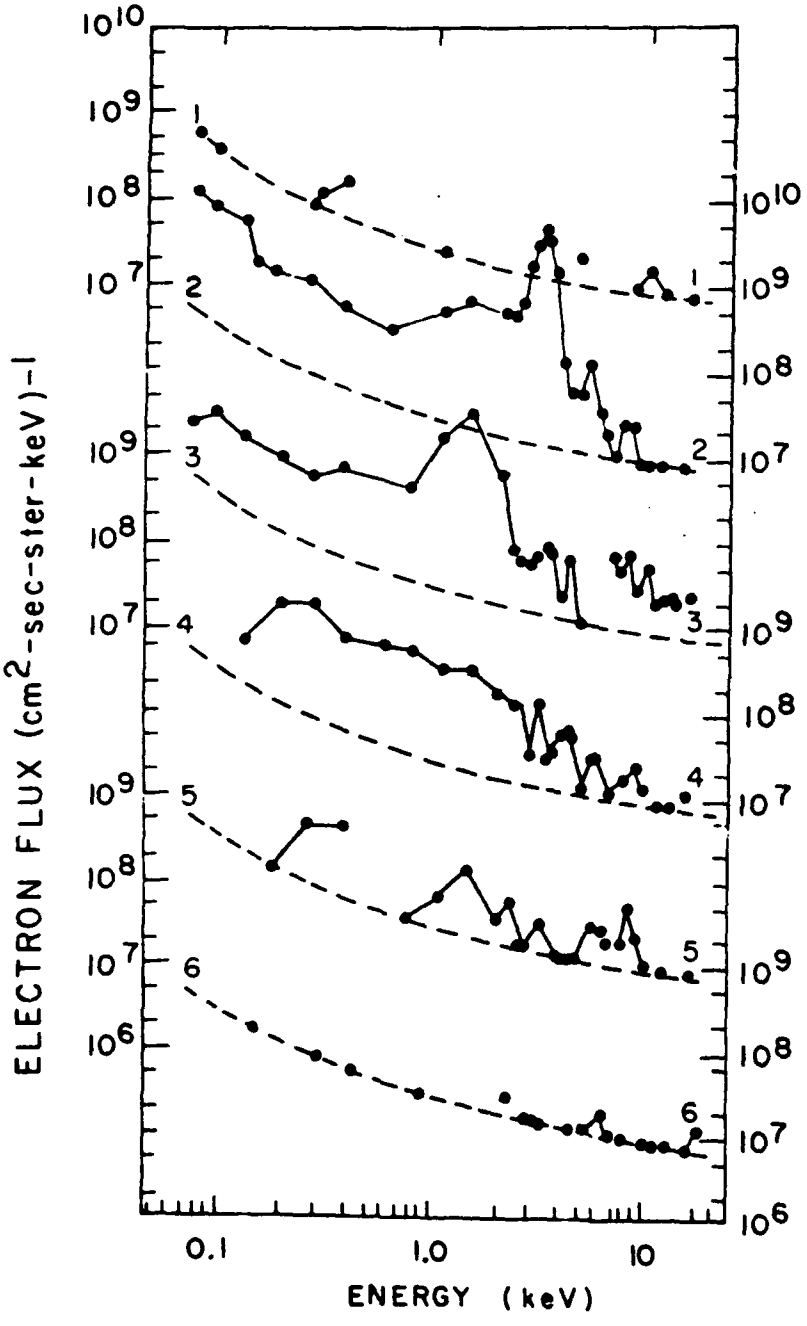

	UT	PITCH ANGLE
1	42495.8	132°
2	42496.8	151°
3	42497.8	171°
4	42498.8	169°
5	42499.9	150°
6	42500.8	131°

Figure 8

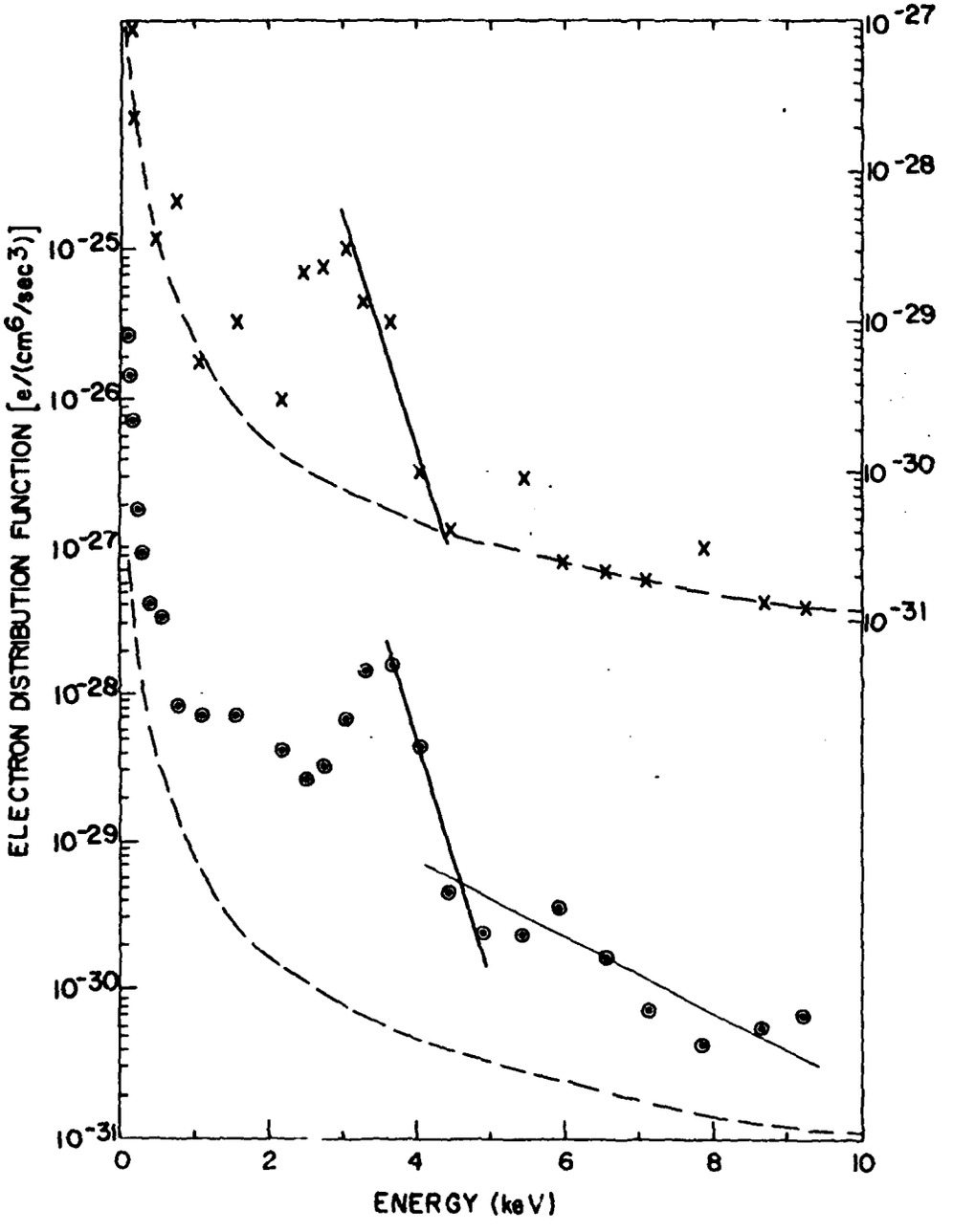
ELECTRON DISTRIBUTION FUNCTION [e/(cm⁶/sec³)]
10⁻²⁵
10⁻²⁶
10⁻²⁷
10⁻²⁸
10⁻²⁹
10⁻³⁰
10⁻³¹
10⁻²⁷
10⁻²⁸
10⁻²⁹
10⁻³⁰
10⁻³¹
0
2
4
6
8
10
ENERGY (keV)

Figure 9

TRITA-EPP-82-15

CIRCUIT EFFECTS ON PIERCE INSTABILITIES, AND DOUBLE-LAYER FORMATION

M.A. Raadu[1] and M.B. Silevitch[2]

November 1982

1) Dept of Plasma Physics
Royal Institute of Technology
S-100 44 Stockholm 70, Sweden

2) Dept of Electrical Engineering
Northeastern University,
Boston, MA 02115, USA

CIRCUIT EFFECTS ON PIERCE INSTABILITIES, AND DOUBLE-LAYER FORMATION

M.A. Raadu and M.B. Silevitch*
Royal Institute of Technology, Department of Plasma Physics,
S-100 44 Stockholm 70, Sweden

Abstract

The role of the Pierce instability in the formation of double layers is considered and compared with that of the Buneman instability. Pierce instabilities have been identified in a double-layer experiment, where they lead to ion trapping. Here the effects of external circuit elements are considered. In the case of immobile ions the onset criteria are unaffected, but in the unstable range the growth rate is reduced by the external impedance. Required experimental values of the circuit elements are estimated. The possible relevance to computer simulations is noted.

* Permanent address: Dept of Electrical Engineering,
Northeastern University, Boston, MA 02115, USA

1. Introduction

Pierce (1944) showed that a finite length system consisting of an electron beam moving through a neutralizing background of fixed ions can be made unstable if the end grids are externally short circuited. If the ions are allowed to respond the instability still occurs (Faulkner and Ware, 1969) and in addition there is an unstable mode depending on ion oscillations which is dominant for long systems and corresponds to the ordinary two-stream Buneman instability. The effects of finite ion mass and of electron thermal velocity spread were treated by Yuan (1977). Saeki et al. (1977) analysed the transition from the Buneman to the Pierce mode with increasing beam current and confirmed their results experimentally. From a nonlinear treatment of the Pierce mode Shapiro and Shevchenko (1967) find that even close to the threshold current the energy of the disturbance becomes comparable with the initial beam energy.

In the long-wavelength regime the ordinary two-stream instability for an unbounded plasma can drive local evacuations, which may initiate the formation of double layers (Raadu and Carlqvist, 1981). The local plasma density in the evacuation region continues to drop even in the non-linear regime as shown by numerical analysis including the ion Vlasov equation (ibid) and in an analytic fluid treatment (Galeev et al., 1981). Quasineutrality holds during the initial evacuation, so that the ion and electron density perturbations are approximately equal. The final formation of a double layer must depend on departures from charge neutrality and possibly on particle trapping as indicated by numerical solutions of the complete Vlasov-Poisson system of equations (Chanteur and Volokhitin, 1982).

Iizuka et al. (1979) have observed the formation of a double layer as the result of the injection of an electron beam into a low density plasma. As they also described in the preliminary report (Saeki et al., 1977) Pierce instabilities supplant the Buneman instability beyond a critical current level. They ascribe the formation of a potential minimum to the rapid growth of the Pierce mode. Ions are trapped in this suddenly formed potential well and constitute the thermal population on the low-potential side of the double layer. Thus in their experiment the Pierce instability plays a vital role in the formation

of the double layer.

The essential difference between the situation considered by Raadu and Carlqvist (1981) and that investigated by Iizuka et al. (1979) is the length of the system. For a long system many unstable Buneman modes are present and the form of the growing perturbations reflects their initial random nature, density depletions leading to local evacuations which may initiate double-layer formation. In a short system a single Pierce mode can dominate and determine the form of the growing perturbation and in particular the tendency to form local evacuation regions is lost.

In view of these considerations it is of interest from the point of view of double-layer formation to look further into the conditions for the growth of the Pierce instability. Here we will investigate the influence of an external circuit with finite impedance instead of the normally assumed zero impedance short-circuit. In a laboratory experiment it is possible to introduce external circuit elements and to influence the growth of Pierce instabilities. In a cosmic plasma an external current system feeding a region of double-layer formation may be represented by an equivalent circuit. In both cases the Pierce instability may be suppressed or at least the growth rate may become insignificant.

2. Influence of an external circuit

In order to highlight the effects of an external circuit we will here only consider the case of a cold electron beam and immobile ions. For an unbounded plasma there are only stable Langmuir modes given by the standard dispersion relation,

$$1 - \frac{\omega_{pe}^2}{(\omega - kv)^2} = 0 \qquad (1)$$

where k and ω are the wave number and frequency, v is the beam velocity and ω_{pe} the plasma frequency. For a finite length system with space coordinate x potential perturbations of the form

$$\phi(x) = [A \exp(ik_+ x) + B \exp(ik_- x) - E_0 x]\, e^{-i\omega t} \qquad (2)$$

become possible where the uniform electric field E_o is due to charges on the end grids (x = o, d) and $k_\pm$ are the solutions of the free-mode equation (1).

At the boundary where the electron beam is injected (x = 0) the density and velocity perturbation are set to zero. Alternative boundary conditions (e.g. setting the electrical field to zero) are in general not acceptable, since they imply a non-physical coupling between the conditions within the plasma region and the parameters of the beam injection mechanism. The electron beam is disturbed by the external circuit only through the uniform electric field E_o. The external circuit which is connected to the end grids responds only to the potential difference $\phi(d) - \phi(0)$. There is no direct coupling between the external current which builds up charges on the end grids and the current carried by the electron beam. This severely restricts the possible applications to cosmic situations where in general the electron current within a region of double-layer formation is, together with the external current, part of the same extended current system and "end grids" which may carry charge do not exist.

In the standard Pierce analysis the two boundary conditions with the short-circuit condition $\phi(d) = \phi(0)$ lead to a characteristic equation determining the growth rate for given plasma parameters (Pierce, 1944; see also Mikhailovskii, 1974). Here we instead consider the external circuit illustrated in Figure 1, consisting of capacitance C, resistance R and inductance L in series. For an external current $I = \dot{Q}$ where $\pm Q$ are the charges on the end grids, the potential across the plasma satisfies

$$\phi(d) - \phi(0) = \frac{Q}{C} + I R + L \frac{dI}{dt} \qquad (3)$$

Introducing the vacuum capacitance of the plasma volume $C_o = \varepsilon_o A/d$ where A is the area of a grid we have from (2)

$$A[\exp(ik_+ d)-1] + B[\exp(ik_- d)-1]$$

$$= \frac{Q}{C_o} + \frac{Q}{C} + I R + L \frac{dI}{dt} \qquad (4)$$

In this form the capacitance C_o enters as a circuit element in series with those in the external circuit and is thus significant for determining their relative importance. Equation (4) together with the standard boundary conditions yields the modified characteristic equation

$$P(\theta) \equiv 2\theta\theta_e^2 [1 - e^{-\theta}\cos\theta_e] + \theta_e(\theta_e^2 - \theta^2) e^{-\theta}\sin\theta_e$$

$$+ [1 + \bar{C}^{-1} + \bar{R}\theta + \bar{L}\theta^2]\ \theta^2(\theta_e^2 + \theta^2) = 0 \qquad (5)$$

where we use Yuan's (1977) notation ($\theta = -i\omega d/v$, $\theta_e = \omega_{pe} d/v$) and have non-dimensionalized the circuit parameters ($\bar{C} = C/C_o$, $\bar{R} = RC_o v/d$, $\bar{L} = LC_o v^2/d^2$). If $\bar{C}^{-1} = \bar{R} = \bar{L} = 0$ we recover the standard characteristic equation.

3. Discussion

We first of all notice that for marginal instability ($\theta = 0$) it follows from Equation (5) that $\theta_e = n\pi$. This condition is identical to the standard case. The marginally unstable modes consist of an integral number of half wave lengths of spacially undamped sinusoidal oscillations with no uniform field component ($E_o = 0$). Clearly the external circuit cannot influence these modes as there is no required external current ($\dot{Q} = 0$).

In the unstable parameter ranges the growth rate θ is reduced by the external impedances. Thus in Figure 2 the effect of an external inductance is shown. For the particular choice $\bar{L} = 40$ the maximum growth rate is reduced by a factor ≈ 0.58 as compared with the case of an external short-circuit.

The growth rate θ decreases rather slowly as the external inductance is increased. This may be seen from Table 1, where the equivalent necessary values of the inductance $\bar{L}$, resistance $\bar{R}$ or capacitance $\bar{C}$ are given for a number of growth rates ($\theta_e = 1.6\pi$). In Equation (5) the circuit parameters appear additively in the same term and hence for a given growth rate it is easy to find parameter values which give the same result. For large values of the impedance we have the approximations,

$$\theta \approx (\alpha/\bar{L})^{-1/4} \equiv (\alpha/\bar{R})^{-1/3} \equiv (\alpha\bar{C})^{-1/2}$$

where $\alpha = -\vartheta_e \sin\theta_e$, which again illustrates the relatively weak dependence on the external circuit parameters.

For the experiment of Saeki et al.(1977; Iizuka et al., 1979) we estimate the vacuum capacitance of the plasma volume to be $C_o \approx 0.25$ pF and the transit time $d/v = 10^{-7}$s. To determine the size of external circuit elements, which according to the theory presented here could have an effect if introduced into the experiments, we note that for the dimensionless parameters $\bar{L}$, $\bar{R}$ and $\bar{C}$ to be equal to unity the actual values should be L = 0.04 H, R = 0.4 MOhm, C = 0.25 pF. In particular for the theoretical curve given in Figure 2 ($\bar{L} = 40$) the corresponding outer inductance would be L = 1.6 H. The required dimensions of the circuit elements are such that unless they are deliberately introduced into the experiment the impedance of the outer circuit has almost certainly a negligible effect in the experiments of Saeki et al. (ibid).

In view of the comments in Section 2 the special configuration required for the Pierce instability is unlikely to be applicable in cosmic situations. However if we estimate the external inductance by $\mu_o \ell$ where ℓ is the length of the current system and consider a local region of length d and cross section d^2 the dimensionless inductance $\bar{L} = (v/c)^2(\ell/d)$. Since $v < c$ and we should have $\ell > d$ there is no a priori restriction on $\bar{L}$. From the analysis presented here we must have $\bar{L} \gg 1$ for a significant reduction of the Pierce instability growth rate.

Finally we note that computer simulations of double-layer formation are of necessity made for a finite length system. Instabilities of the Pierce type are then possible and may then be suppressed by including the effects of a suitable external circuit in the simulation. A modified form of the Pierce instability might be expected for example if a constant voltage is imposed across the simulation region (cf. Smirnov, 1966). This implies that the perturbations in the total potential difference must be zero and an appropriate uniform electric field must be superimposed as in the standard Pierce instability analysis.

4. Acknowledgements

The authors would like to thank L. Lindberg and S. Torvén for their interest in this work. This work was supported by the Natural Science Research Council and for one of us (M.B. Silevitch) also by AFOSR grant 78-3731.

References

Chanteur, G. and Volokhitin, A.S.: 1982, to be presented at First International School for Space Simulations, Kyoto, Japan, Nov. 1-12, 1982.

Faulkner, J.E. and Ware, A.A.: 1969, The Effect of Finite Ion Mass on the Stability of a Space-Charge-Neutralized Electron Beam, J. Appl. Phys. 40, 366.

Galeev, A.A., Sagdeev, R.Z., Shapiro, V.D. and Shevchenko, V.I.: 1981, The Nonlinear Theory of the Buneman Instability, Sov. Phys. JETP 54, 306.

Iizuka, S., Saeki, K., Sato, N. and Hatta, Y.: 1979, Buneman Instability, Pierce Instability and Double-Layer Formation in a Collisionless Plasma, Phys. Rev. Lett. 43, 1404.

Mikhailovskii, A.B.: 1974, Theory of Plasma Instabilities Vol. 1, Consultants Bureau, New York, p. 20.

Pierce, J.R.: 1944, Limiting Stable Current in Electron Beams in the Presence of Ions, J. Appl. Phys. 15, 721.

Raadu, M.A. and Carlqvist, P.: 1981, Electrostatic Double Layers and a Plasma Evacuation Process, Astrophys. Space Sci. 74, 189.

Saeki, K., Iizuka, S., Sato, N. and Hatta, Y.: 1977, Buneman Instability and Current Limitation in a Bounded and Magnetized Plasma, in Proc. of the Thirteenth Int. Conf. on Physics of Ionized Gases, Berlin, September 1977, Phys. Soc. German Democratic Republic, Leipzig, p. 783.

Shapiro, V.D. and Shevchenko, V.I.: 1967, Contribution to the Nonlinear Theory of Instability of an Electron Beam in a System with Electrodes, Sov. Phys. JETP 25, 92.

Smirnov, V.M.: 1966, Instability of Nonlinear Stationary Potential Oscillations in Electron-Ion Beams, Sov. Phys. JETP 23, 668.

Yuan, K.: 1977, Note on the Effects of Finite Ion Mass and Electron Thermal Velocity Spread on the Aperiodic Instabilities of a Space-Charge-Neutralized Electron Beam in a Planar Diode, J. Appl. Phys. 48, 133.

Table 1

Values of the nondimensionalized inductance $\bar{L}$, resistance $\bar{R}$ and capacitance $\bar{C}$, each of which give the same growth rate θ (= -ikd/v) if included in the outer circuit. The electron beam density is such that θ_e (= $\omega_{pe}d/v$) = 1.6π and $\theta(\theta_e)$ is close to the first maximum. For given θ, $\bar{R} = (\theta\bar{C})^{-1} = \theta\bar{L}$.

			$\theta_e = 1.6\pi$
θ	$\bar{L}$	$\bar{R}$	$\bar{C}$
·810	0	0	∞
·75	1.09	·816	1.63
·5	28.6	14.3	·140
·25	835	209	·0192
·1	41700	4170	·0024

Figure Captions

Fig. 1. The physical system. An electron beam (e^-) traverses a region of stationary ions bounded by grids (located at $x = 0, d$) carrying charges $\pm Q$. The charges are supplied via an external circuit with current I passing capacitance C, resistance R and inductance L in series.

Fig. 2. The dimensionless growth rate $\theta(= -i\omega d/v)$ is given as a function of the electron-beam parameter ϑ_e $(= \omega_{pe} d/v)$ for the case of an external dimensionless inductance $\bar{L} = 40$, solid curve, and for comparison for the case of an external short-circuit ($\bar{L} = 0$), dashed curve.

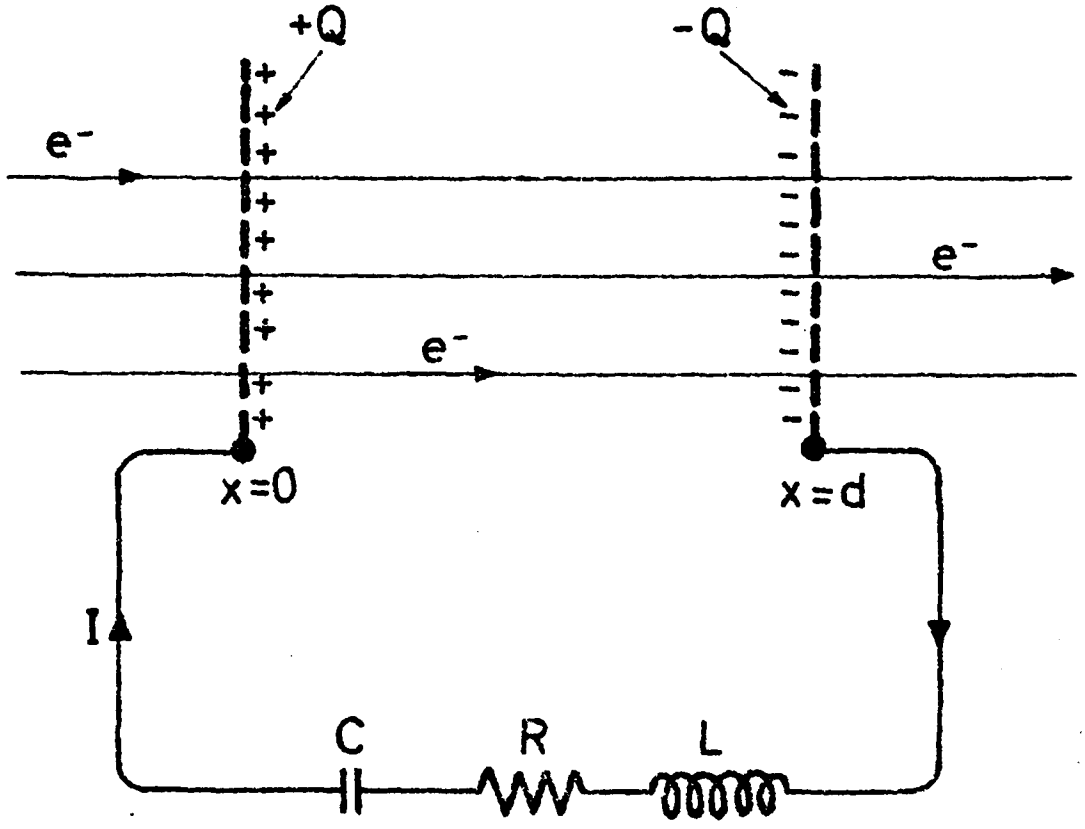

Fig. 1

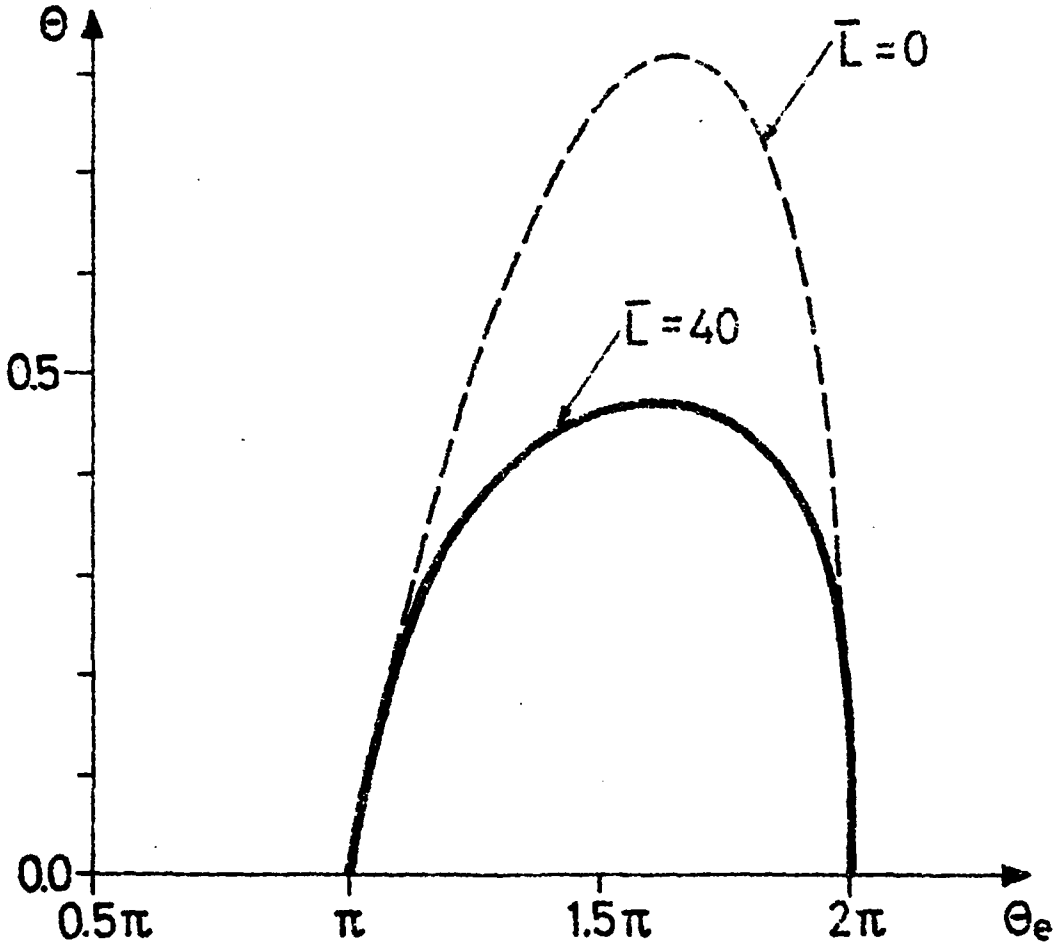

Fig. 2

TRITA-EPP-82-15 ISSN 0348-7539

Royal Institute of Technology, Department of Plasma Physics,
S-100 44 Stockholm 70, Sweden

CIRCUIT EFFECTS ON PIERCE INSTABILITIES, AND DOUBLE-LAYER FORMATION

M.A. Raadu and M.B. Silevitch*
November 1982, 12 pp. incl. illus., in English

The role of the Pierce instability in the formation of double layers is considered and compared with that of the Buneman instability. Pierce instabilities have been identified in a double-layer experiment, where they lead to ion trapping. Here the effects of external circuit elements are considered. In the case of immobile ions the onset criteria are unaffected, but in the unstable range the growth rate is reduced by the external impedance. Required experimental values of the circuit elements are estimated. The possible relevance to computer simulations is noted.

Key words: Double layers, Pierce instability, Growth rates, Circuit effects, Buneman instability, Bounded plasma, Electron beams.

* Permanent address: Dept of Electrical Engineering, Northeastern University, Boston, MA 02115, USA

TRITA-EPP-82-12

ON THE NEGATIVE RESISTANCE OF DOUBLE LAYERS

M.A. Raadu[1] and M.B. Silevitch[2]

August 1982

1) Dept. of Plasma Physics
Royal Institute of Technology
S-100 44 Stockholm 70, Sweden

2) Dept.of Electrical Engineering
Northeastern University, Boston
MA 02115, USA

ON THE NEGATIVE RESISTANCE OF DOUBLE LAYERS

M.A. Raadu and M.B. Silevitch*

Royal Institute of Technology, Department of Plasma Physics,
S-100 44 Stockholm 70, Sweden

Abstract

It is known that large amplitude oscillations can occur in the current flowing through a plasma diode, typically when a constant potential is applied across the device. Burger (1965) suggested via a computer simulation that the oscillation characteristics was a function of the quantities τ_e and τ_i, namely the respective time for an electron and an ion to cross the electric field region inside the diode. On the rapid time scale τ_e, the self consistent equilibrium configuration, was unstable. Norris (1964) had previously arrived at the same conclusion using analytical arguments. In that work, it was concluded that the instability occurred since the diode acted as a negative resistance on the τ_e scale. A positive feedback effect forced the system away from equilibrium.

Silevitch (1981) used the Burger mechanism to suggest an explanation for the flickering aurora phenomenon. He extended the Norris argument and showed by a variational method that a plausible analytic model for a double layer (DL) behaved as a negative resistance on the τ_e scale. In this present work we re-examine the negative resistance calculation by taking a more detailed account of the constraints which are imposed on the electron distributions that exist in the DL region. Specifically, we shall focus upon the role of the energetic trapped electrons which originate at the high potential side of the DL.

*Permanent address: Dept of Electrical Engineering,
Northeastern University, Boston, MA 02115, U.S.A.

is indeed proportional to the time for an ion to traverse a distance which is characterized by the spatial extent of the entire system (i.e. the electrode separation distance). This is in contrast to the suggestion of Silevitch (1981) (henceforth referred to as Paper 1) that the transit distance comprise only the narrow DL region.

In this present work we shall focus upon the dynamics of the DL on the τ_e time scale. We will reexamine the computation of negative resistance given in Paper 1 by taking a more detailed account of the constraints which are imposed on the various electron distributions which exist within the DL region. It should also be emphasized that the DL instability discussed here is a global rather than a local effect. By this we mean that the properties of the external circuit surrounding the DL element play a crucial role in the devlopment of the relaxation oscillations. Thus in a given application it is not enough to determine that the DL behaves as a negative resistor on the τ_e scale. One must also examine how this resistance couples through an external circuit and whether it causes a positive feedback effect.

As in Paper 1 we shall choose a particular steady state DL model and demonstrate that it exhibits a negative resistance on the τ_e time scale. In our case we continue using the Kan and Lee (1980) model introduced in Paper 1. It is intended that the calculation presented here be used as a guide if one wants to investigate the stability of a different DL model that may better describe some particular experimental situation.

A similar but somewhat abbreviated version of this paper, Raadu and Silevitch (1982), will appear as part of the proceedings of a small symposium. We are presenting the results again here because the earlier version will not be widely circulated within the plasma physics community. Moreover we will make extensive use of the material already contained in Paper 1, in order to avoid unneccessary mathematical detail.

In Section 2 we present a summary of the Kan and Lee (1980) DL model. We examine the perturbation of the DL on the τ_e time scale in Section 3. The variational technique given in Paper 1 is generalized and we compute the negative resistance of the DL which results when various constraints are imposed on the

electron distribution functions. It is also found that the immobile ions introduce an additional term in the perturbation expansion that was overlooked in Paper 1. We investigate this term in Section 4 and present arguments to show that it has a negligible effect on the results presented here and in Paper 1.

2. Equilibrium model

The equilibrium auroral DL model used in Paper 1 is taken from the work of Kan and Lee (1980) . The DL potential structure $\phi(x)$, varies from $\phi(x=0) = 0$ to $\phi(x=d) = \phi_o$. Moreover, as shown in Figure 4 of Paper 1, there are three distinct electron populations associated with the Kan and Lee DL model. These are:

(a) Streaming electrons originating at $\phi(x=0) = 0$

A waterbag velocity distribution is chosen for this population which is simply

$$f_{el}(\phi) = f_1 = \frac{N_{el}}{2V_{el}} , \quad V_\ell(\phi) < v < V_u(\phi) \tag{1}$$

where $V_\ell(\phi) = (2|e|\phi/m)^{\frac{1}{2}}$ and $V_u(\phi) = [4V_{el}^2 + V_\ell^2(\phi)]^{\frac{1}{2}}$. Here N_{el} and V_{el} are the density and streaming velocity of the electrons originating at $x = 0$. Following Paper 1 we can easily obtain expressions for the electron density, $n_{el}(\phi)$ and its integral $g_{el}(\phi) \equiv \int_{\bar{\phi}=o}^{\phi} n_{el}(\bar{\phi})d\bar{\phi}$ at any point $\phi(x)$ within the DL region. Note that it would be more precise to indicate these quantities as functionals of $f_{el}(N_{el}, V_{el}, \phi, v)$.

(b) Trapped degraded primary and secondary electrons originating at $\phi(x=d) = \phi_o$

Again for these particles we use a waterbag distribution f_{et} of value f_t centered at $v = 0$ and cut off at $v = \pm(2|e|\phi/m)^{\frac{1}{2}}$. Thus,

$$f_t = \frac{N_{et}}{2}\left(\frac{m}{2|e|\phi_o}\right)^{\frac{1}{2}} \tag{2}$$

where N_{et} is the density of these trapped electrons at $x = d$. Again simple expressions for $n_{et}(\phi)$ and $g_{et}(\phi)$ can be obtained (see Paper 1).

(c) Trapped low energy electrons originating at $\phi(x=d) = \phi_o$

A Maxwellian distribution is assumed for this population. It is a full range function characterized by the parameters $N_{eo}(>>N_{el})$ and $kT_{eo}(<<|e|\phi_o)$ which respectively represent the electron den-

sity and thermal energy at x = d.

3. Perturbation Analysis

If the equilibrium DL structure is perturbed on the τ_e time scale then the dynamic resistance of the DL is defined as

$$R_D = \frac{\delta\phi_o}{\delta j}(A)^{-1} . \qquad (3)$$

Here A is the DL cross sectional area and δj ($\delta\phi_o$) represents the electron current density (potential) variations from the equilibrium values

[i.e. $\phi(x) \xrightarrow{\text{perturbation}} \phi^*(x) = \phi(x) + \delta\phi(x)$]. Cleary only the electrons in category (a) contribute to j and thus,

$$\delta j = \delta(|e|N_{el}V_{el}) = |e|V_{el}\delta N_{el} + |e|N_{el}\delta V_{el} \qquad (4)$$

In order to calculate R_D we need the key result

$$0 = \delta\{g_{el} + g_{et} + g_{eo}\} \qquad (5)$$

This equation is obtained by first multiplying Poisson's equation by $d\phi/dx$ and then integrating from x = 0 to x = d assuming charge neutrality at both endpoints. Finally, the same procedure is repeated for the perturbed state (ϕ^*) and the two equations are subtracted keeping only first order terms in the variations like $\delta\phi$. It should be noted that to this order in $\delta\phi$ it is not neccessary to impose strict charge neutrality for the perturbed state at x = 0, d. Moreover, a rigorous derivation of (5) would include on the rhs a static ion term δG_{ion} defined by

$$\delta G_i \equiv -\int_{x=0}^{d} dx\, n_i(x)\left[\frac{d\phi^*}{dx} - \frac{d\phi}{dx}\right] \qquad (6)$$

where $n_i(x)$ is the ion density profile in the unperturbed state. In Paper 1 this term was neglected. An argument justifying this approximation is presented in the final portion of this paper.

In order to obtain an expression for R_D we need to specify in detail those constraints that apply during the initial disruption. To illustrate this consider electron population (a). Eq. (4) defines a relation between δN_{el} and δV_{el}. Another is needed. For example, in Paper 1 it was assumed that N_{el} and V_{el} were independent and so either $\delta N_{el} = 0$ (i.e. strict charge neutrality) or $\delta V_{el} = 0$. Perhaps a more realistic constraint would be to impose the condition $\delta f_1 = 0$. This would imply from

Eq. (1)

$$0 = \delta N_{el} - \frac{N_{el}}{V_{el}} \delta V_{el} \quad . \tag{7}$$

From Eqs. (4) and (7) we find

$$\delta N_{el} = \tfrac{1}{2} \frac{\delta j}{|e| V_{el}} \quad , \quad \delta V_{el} = \tfrac{1}{2} \frac{\delta j}{|e| N_{el}} \quad . \tag{8}$$

The expression for R_D is now obtained by expanding Eq. (5) as:

$$0 = [\frac{\partial g_{el}}{\partial N_{el}} \delta N_{el} + \frac{\partial g_{el}}{\partial V_{el}} \delta V_{el} + \frac{\partial g_{et}}{\partial N_{et}} \delta N_{et} + \frac{\partial g_{eo}}{\partial N_{eo}} \delta N_{eo} + \Delta \delta \phi_o] \tag{9}$$

where $\Delta \equiv \frac{\partial g_{el}}{\partial \phi_o} + \frac{\partial g_{et}}{\partial \phi_o} + \frac{\partial g_{eo}}{\partial \phi_o}$. Let us first follow Paper 1 by assuming $\delta N_{el} = \delta N_{et} \equiv \delta N_{eo} \equiv 0$. Note that these constraints would not impose strict charge neutrality at x = d. Using Eqs. (4) and (9) we obtain the resistance R_1 given by

$$R_1 = -(\Delta N_{el} |e| A)^{-1} \frac{\partial g_{el}}{\partial V_{el}} \tag{10}$$

If we replace $\delta N_{el} = 0$ by condition (7) we find the DL negative resistance R_2 will have the value R_2 where

$$R_2 = -(2A|e|\Delta)^{-1} [\frac{\partial g_{el}}{\partial N_{el}} \frac{1}{V_{el}} + \frac{\partial g_{el}}{\partial V_{el}} \frac{1}{N_{el}}] \tag{11}$$

For the parameters of the auroral example in Paper 1 we find that the two terms in the bracket have roughly the same magnitude and hence $R_2 \approx R_1$.

Let us now generalize the constraints on δN_{et} and δN_{eo}. An obvious first step is to assume strict charge neutrality at $\phi = \phi_o$. This would imply

$$-\delta n_{el}(\phi_o) = \delta N_{et} + \delta N_{eo} \tag{12}$$

For simplicity let us also still assume $\delta N_{el} = \delta N_{eo} = 0$. From Eqs. (4) and (12) we find that

$$\delta N_{et} = -\{(N_{el}|e|)^{-1} \frac{\partial n_{el}}{\partial V_{el}} \delta j + \frac{\partial n_{el}}{\partial \phi_o} \delta \phi_o\} \tag{13}$$

the DL negative resistance will now have the value R_3 given by:

$$R_3 = -(N_{el}|e|A)^{-1}\left[\Delta - \frac{\partial g_{et}}{\partial N_{et}} \frac{\partial n_{el}}{\partial \phi_o}\right]^{-1}\left[\frac{\partial g_{et}}{\partial V_{el}} - \frac{\partial g_{et}}{\partial N_{et}} \frac{\partial n_{el}}{\partial V_{el}}\right] \quad (14)$$

For the parameters of the auroral DL of Paper 1 we find that only the $\delta n_{el}/\delta V_{el}$ correction term is important and

$$R_3 \approx \frac{1}{4} R_1 \quad (15)$$

Moreover, if we assumed that is was primarily the low energy population which reacted to maintain charge neutrality (i.e. $\delta N_{et} = 0$, $\delta N_{eo} = -\delta n_{el}(\phi_o)$), then the resulting negative resistance would be approximately equal to R_1. A result similar to Eq. (15) is obtained if we relax the charge neutrality constraint and assume instead $\delta f_t = \delta N_{eo} = 0$.

From the above discussion we conclude that the response of the trapped particle populations will have quite an important effect upon the value of DL negative resistance. According to the theory in Paper 1 a smaller value of negative resistance could quench the DL disruption on the τ_e time scale. To test this hypothesis we can envisage an experiment which allows the controlled injection of trapped electrons. One could then study the DL disruption characteristics as a function of the trapped electron distributions.

4. Approximate Treatment of Unperturbed Ions

Before concluding this paper we will justify the neglect of δG_i (Eq. (6)) in Eq. (5). The unperturbed electric field of a strong DL structure is primarily nonzero in an interior region of space $\Delta x (< d)$. Under the assumption that the perturbed electric field $(\frac{-d\phi^*}{dx})$ is also confined to essentially the same Δx region we can rewrite Eq. (6) as,

$$\delta G_i \approx \bar{n}_i \int_0^d dx \frac{d}{dx}(\phi^* - \phi) = \bar{n}_i \, \delta\phi_o .$$

Here $\bar{n}_i$ is a mean value of unperturbed ion density in the Δx region It is given by the expression,

$$\bar{n}_i = \frac{1}{\phi_o} \int_{x=0}^{d} dx \, n_i(x) \frac{d\phi}{dx} = \frac{1}{\phi_o} G_i(\phi_o) .$$

For the auroral DL model discussed in Paper 1, it can be shown that $\bar{n}_i \sim 0.1 \, (\partial g_e/\partial \phi_o)$ and so for this case δG_i can indeed

be neglected in Eq. (5).

Acknowledgement. The authors would like to thank L.P. Block, C.-G. Fälthammar, L. Lindberg and S. Torvén for their stimulating discussions during the course of this work. This work was supported by the Natural Science Research Council and for one of us (M.B. Silevitch) also by AFOSR grant 78-3731.

References

Burger, P., Theory of large amplitude oscillations in the one-dimensional cesium thermionic converter, J. Appl. Phys., 36, 1938, 1965.

Iizuka, S., Michelsen, P., Rasmussen, J.J., Schrittwieser, R., Hatakeyama, R., Saeki, K. and Sato, N., Dynamics of a potential barrier formed on the tail of a moving double layer in a collisionless plasma, Phys. Rev. Lett., 48, 145, 1982a.

Iizuka, S., Michelsen, P., Rasmussen, J.J., Schrittwieser, R., Hatakeyama, R., Saeki, K., Sato, N., Dynamical evolution of double layers in a collisionless plasma, Proceedings of the 1982 Int. Conf. on Plasma Physics, Göteborg, June 9-15, p. 134, 1982b.

Kan, J.R. and Lee, L.C., On the auroral double layer criterion, J. Geophys. Res., 85, 788, 1980.

Norris, W.T.,Nature of spontaneous oscillations in a cesium diode energy converter, J. Appl. Phys., 35, 3260, 1964.

Raadu, M.A. and Silevitch, M.B., On the negative resistivity of double layers, paper presented at the Symposium on Plasma Double Layers, Risø, June 16-18 (to be published as a Risø report), 1982.

Silevitch, M.S., On a theory of temporal fluctuations in the electrostatic potential structures associated with auroral arcs, J. Geophys. Res., 86, 3573, 1981.

Singh, N. and Schunk, R.W., Current carrying properties of double layers and low frequency auroral fluctuations, Geophys. Res. Lett 9. 446, 1982.

Torvén, S. and Babić, M., Current chopping space charge layers in a low pressure arc plasma, Twelfth Int. Conf. on Phenomena in Ionized Gases, p. 124, 1975.

TRITA-EPP-82-12

Royal Institute of Technology, Department of Plasma Physics
S-100 44 Stockholm 70, Sweden

ON THE NEGATIVE RESISTANCE OF DOUBLE LAYERS

M.A. Raadu and M.B. Silevitch*

August 1982, 8 pp., in English

Abstract

It is known that large amplitude oscillations can occur in the current flowing through a plasma diode, typically when a constant potential is applied across the device. Burger (1965) suggested via a computer simulation that the oscillation characteristics was a function of the quantities τ_e and τ_i, namely the respective time for an electron and an ion to cross the electric field region inside the diode. On the rapid time scale τ_e, the self consistent equilibrium configuration, was unstable. Norris (1964) had previously arrived at the same conclusion using analytical arguments. In that work, it was concluded that the instability occurred since the diode acted as a negative resistance on the τ_e scale. A positive feedback effect forced the system away from equilibrium.

Silevitch (1981) used the Burger mechanism to suggest an explanation for the flickering aurora phenomenon. He extended the Norris argument and showed by a variational method that a plausible analytic model for a double layer (DL) behaved as a negative resistance on the τ_e scale. In this present work we re-examine the negative resistance calculation by taking a more detailed account of the constraints which are imposed on the electron distributions that exist in the DL region. Specifically, we shall focus upon the role of the energetic trapped electrons which originate at the high potential side of the DL.

Key words: Double Layers, Stability, Negative Resistance, Relaxation Oscillations, Stationary Ions.

*Permanent adress: Dept. of Electrical Engineering, Northeastern University, Boston, MA 02115, U.S.A.

Second Order Effects Related to a Model for a Parallel Shock

by

R. W. Jackson

Northeastern University

April 27, 1982

Abstract

Second order effects are calculated for a low frequency electromagnetic instability due to an ion beam in a plasma. This instability is a characteristic of a parallel shock model which includes an ion reflecting electrostatic sub-shock. The analysis is similar to that done by S. P. Gary but a counterstreaming configuration is chosen which is homogeneous in time and which has spacially growing modes. Among other effects, energy is transferred from the incoming main plasma ions to the beam ions. Electron pressure effects are calculated and are small for low frequencies. The application of this model to the earth's bow shock is discussed.

1. Introduction

A shock model which consists of an ion reflecting potential barrier immersed in electromagnetic turbulence has been suggested in theory [Jackson and Golden, 1979] and by computer simulation of oblique shocks [Lindman and Drummond, 1971; Biskamp and Welter, 1972]. The simulation results of Lindman and Drummond indicate the formation of an ion reflecting potential barrier which they associate with the ion acoustic wave. This barrier reflects ions upstream causing a streaming electromagnetic instability which is identified by the authors as a whistler instability ($\omega >> \Omega_i$). In a later simulation, Biskamp and Welter note that this whistler instability stabilizes by rearranging the electron distribution and not the ion distribution. They suggest that the ions are thermalized by the occurrence of a nonlinear two-stream ion acoustic instability which could be triggered by potential variations. This instability would then heat the ions. As the oblique shock becomes more parallel, the high frequency whistler instability used by these authors becomes stable. It was later shown [Jackson and Golden, 1979] that for parallel shocks the low frequency whistler ($\omega \tilde{<} \Omega_i$) streaming instability takes the place of the high frequency whistlers used in the oblique case.

We note further that the reflecting potential model extends the high beta parallel shock model of Kennel and Sagdeev [1967] to the lower beta (~0(1)) range. In the Kennel-Sagdeev model a relatively long scale length potential barrier causes an ion

pressure anisotropy which drives Alfvén waves unstable. For lower beta, the firehose instability is no longer dominant. In addition, the potential barrier becomes more narrow and greater in magnitude due to the increase in shock speed relative to the ion acoustic speed ($C_s^2 = \kappa T_e/m_i$). It is suggested here that this larger potential reflects ions into the upstream region and that the firehose, fluid, Alfvén instability is replaced by a two-stream, low frequency, whistler instability.

This paper is an examination of the second order effects of the low frequency turbulence in the reflected ion shock model. It is similar to the work of Barnes [1970] but the energy and momentum transfers between each fluid are examined in more detail and the second order electric field is retained. First we review the notation and the linear theory. Then the second order effects are calculated for spacially growing modes having time independent average properties. The effect of this turbulence on the pre-barrier plasma is analyzed using the second order theory of Gary and Feldman [1978; Gary, 1978]. Their theory for temporal growth is modified here for the case of spacially growing modes and warm electrons. Also, the expressions derived do not require the assumption $\omega << \Omega_i$ which was used by Gary [1978]. Finally, the similarities between this model and observations of the earth's bow shock are noted.

2. Linear Analysis

In our previous work we supposed the existence of a potential barrier which reflects a small number of ions into the

pre-barrier region. These reflected ions counterstream with the incoming plasma ions causing a resonant low frequency whistler instability. The linear stability analysis assumed a locally homogeneous plasma where modes may grow in time. Low frequency whistlers become unstable for Alfvén Mach numbers greater than about 1.5 if it is assumed that: (i) the ion acoustic soliton is the reflecting potential, (ii) the Alfvén and ion acoustic speeds are equal, and (iii) electron trapping in the potential is allowed.

It is assumed that this very steep potential barrier exists at a point $z = 0$ (see Figure 1) and reflects a small amount of the cool incoming plasma into the upstream region ($z < 0$) along a constant magnetic field, $\vec{B}_o = B_o \hat{z}$. At the point $z = 0^-$, the *reflecting* potential is assumed to be zero. The ion distribution which results would then be similar to Figure 2 where $v_m = (2e\,\phi_m/m_i)^{1/2}$ and ϕ_m is the maximum potential of the barrier.

Using this ion distribution in the kinetic dispersion relation for $\vec{k} || \vec{B}_o$, we make the following assumptions: (i) the incoming ion stream and the electrons appear cold to the unstable waves, (ii) $|\omega| << |\Omega_e|$, (iii) charge and current neutrality, (iv) $\eta << 1$ (η represents the fraction of incoming ions which are reflected). This results in the expression for the temporal growth rate,

$$\gamma = \frac{\pi^2 \nu(\nu - kV_u + \Omega_i)^2 \Omega_i}{n_o|k|(\nu - kV_u)(\nu - kV_u + 2\Omega_i)}$$

$$\cdot \int_0^\infty dv_\perp \, v_\perp^2 \left[\left(1 - \frac{kv_z}{\nu}\right)\frac{\partial}{\partial v_\perp} + \frac{kv_\perp}{\nu}\frac{\partial}{\partial v_z}\right] f_r(v_z, v_\perp, z)\Big|_{v_z=\frac{\nu+\Omega_i}{k}} \tag{1}$$

where V_u is the velocity of the incoming ion stream, f_r is the distribution of the reflected ions limited to the values of v_z such that $-v_m < v_z < 0$, and ν is the real frequency defined by

$$x^2 - \frac{\nu}{\Omega_i} + x\,M_a + 1 - \frac{1}{\left(\frac{\nu}{\Omega_i} - x\,M_a + 1\right)} = 0 \tag{2}$$

with $x = k\,C_a/\Omega_i$ and $M_a = V_u/C_a$. As stated previously, it has been shown that γ is positive for $M_a > 1.5$. For lower Mach numbers the wave resonant velocity, $(\nu + \Omega)/k$, is such that no reflected particles resonate. Please see Jackson and Golden [1979] for details.

For the case where weak spacial growth occurs, the wave vector, k, is complex and the wave frequency real. Defining $k(\omega) = k_r(\omega) + i\,k_i(\omega)$ and assuming $|k_i| << |k_r|$, the expression for k_i in terms of the previously determined γ is

$$k_i(\omega) = - \left. \frac{\gamma(\nu,k)}{v_g(\nu,k)} \right|_{\substack{\nu=\omega \\ k=k_r(\omega)}}$$

and v_g is the wave group velocity. Note that in order for k_i to be small v_g must be finite. The linear analysis indicates that unstable waves occur for waves with (ω, k_r) in the range, $0 > (\omega + \Omega_i)/k_r > - v_m$. For sufficiently large M_a ($M_a > 2.6$ for the ion acoustic soliton with trapped electrons) the portion of the (ω, k_r) dispersion curve which contains zero group velocity whistlers drops out of this range. Two bands occur in the spectrum of unstable whistlers, one having negative group velocities and one with positive group velocities. The whistlers in the first are excited at $z = 0^-$ and grow while propagating in the $-\hat{z}$ direction. The second band of whistlers are excited upstream and grow while being convected downstream through the reflected beam to the point $z = 0^-$. These waves occur at smaller values of $|k_r|$ than the negative moving waves and will have larger growth rates (since the expression for γ has a $|k_r|$ in the denominator). Therefore, the upstream moving modes will be neglected in the following analysis.

3. Second Order Effects

In this section, the effect of growing whistler modes on the background plasma is analyzed. The development is analogous to the second order theory of Gary and Feldman [1978] except that here the spacial evolution of a time average distribution

is examined whereas Gary analyzes the temporal growth of a spacially averaged distribution. There are some interesting differences.

Starting from the kinetic equation in one spacial dimension,

$$\left[\frac{\partial}{\partial t} + v_z \frac{\partial}{\partial z} + \frac{q_j}{m_j}\left(\vec{E} + \frac{\vec{v} \times \vec{B}}{c}\right) \cdot \frac{\partial}{\partial \vec{v}}\right] f_j(z,\vec{v},t) = 0 \qquad (3)$$

and Maxwell's equations,

$$\hat{z} \frac{\partial}{\partial z} \times \vec{E} = -\frac{1}{c} \frac{\partial \vec{B}}{\partial t} \qquad (4)$$

$$\hat{z} \frac{\partial}{\partial z} \times \vec{B} = 4\pi \sum_j \int d^3v \, q_j \, \vec{v} \, f_j + \frac{1}{c} \frac{\partial \vec{E}}{\partial t} \qquad (5)$$

we assume that

$$f_j(z,\vec{v},t) = \langle f_j(z,\vec{v}) \rangle + \delta f_j(z,\vec{v},t) \qquad (6)$$

$$\vec{E}(z,t) = \langle \vec{E}(z) \rangle + \delta \vec{E}(z,t) \qquad (7)$$

$$\vec{B} = B_o \hat{z} + \langle \vec{B}(z) \rangle + \delta\vec{B}(z,t) \tag{8}$$

where the brackets indicate time average. Using (6)-(8) and time averaging (1)-(3) we arrive at

$$\left[v_z \frac{\partial}{\partial z} + \frac{q_j}{m_j} \langle E_z(z) \rangle \frac{\partial}{\partial v_z} \right] \langle f_j(z,\vec{v}) \rangle$$

$$= \frac{-q_j}{m_j} \left\langle \left(\delta\vec{E} + \frac{\vec{v} \times \delta\vec{B}}{c} \right) \cdot \frac{\partial}{\partial \vec{v}} \delta f_j \right\rangle \tag{9}$$

$$\frac{\partial}{\partial z} \langle E_z(z) \rangle = \sum_j 4\pi \, q_j \langle f_j(z,\vec{v}) \rangle \tag{10}$$

where, as Gary points out, the second order field term, $\langle E_z \rangle$ must be retained. Note that the perpendicular components of $\langle \vec{E} \rangle$ are zero if so upstream. Furthermore, since the right hand side of (9) turns out to be ϕ independent (ϕ is the cylindrical velocity variable), it is also consistent to set $\langle \vec{B} \rangle$ equal to zero.

One determines δf_j, $\delta\vec{E}$, $k(\omega)$ in the usual manner by subtracting (9) from (3) and neglecting terms like $\delta f \delta\vec{E}$, $\langle E_z \rangle \delta f$, and higher order terms. Fourier transforming the result with respect to time results in

$$\left[-i\omega + v_z \frac{\partial}{\partial z} - \Omega_j \frac{\partial}{\partial \phi}\right] \delta f_j(\vec{v}, z, \omega) = \frac{-q_j}{m_j}\left[\delta\vec{E}(z,\omega) + \frac{\vec{v} \times \delta\vec{B}(z,\omega)}{c}\right] \cdot \frac{\partial}{\partial \vec{v}} \langle f_j(z,\vec{v})\rangle . \quad (11)$$

The turbulent fields are assumed to have the form,

$$\delta\vec{E}(z,\omega) = \frac{\delta E^{\pm}(o^-,\omega)}{\sqrt{2}} (\hat{x} \mp i\hat{y}) \exp\left[\int_{o^-}^{z} ik(u,\omega)\,du\right]. \quad (12)$$

where $\delta E^{\pm}(o^-,\omega)$ is the spectrum of whistlers at $z = o^-$. The reader is reminded that these whistlers are excited upstream (where the plasma is assumed to be in a marginally stable

state) and grow as they are convected back toward $z = o^-$. Using (12) in (11), solving for δf_j and combining the results with Maxwell's equations gives the dispersion relation for $k(z,\omega)$

$$D^{\pm}(k,\omega) = \frac{k^2c^2}{\omega^2} - \sum_j \frac{\omega_{pj}^2}{2n_j\omega} \int d^3v\, v_\perp \frac{[(1 - \frac{kv_z}{\omega})\frac{\partial}{\partial v_\perp} + \frac{kv_\perp}{\omega}\frac{\partial}{\partial v_z}]\langle f_j(z,\vec{v})\rangle}{\omega - kv_z \mp \Omega_j}$$

$$= 0 \qquad (13)$$

which is valid for regions for enough upstream from o^- that ballistic terms phase mix out. This requires that the spread in reflected beam velocity be large enough so that

$$|k_i^{-1}(\omega \mp \Omega_j)\Delta(\frac{1}{v_z})| >> |. \qquad (14)$$

The approximate solution of (13) for $k(\omega,z)$ has been discussed in the previous section.

$$\text{R.H.S. of (9)} = \text{Im}\left\{\frac{-q_j^2}{m_j^2}\int_{-\infty}^{\infty} d\omega \left|\delta E^-(\omega,z)\right|^2 \cdot \left[\left(1-\frac{k^{-*}v_z}{\omega}\right)\frac{1}{v_\perp}\frac{\partial}{\partial v_\perp}v_\perp + \frac{k^{-*}v_\perp}{\omega}\frac{\partial}{\partial v_z}\right] \cdot \frac{\left[\left(1-\frac{k^- v_z}{\omega}\right)\frac{\partial}{\partial v_\perp} + \frac{k^- v_\perp}{\omega}\frac{\partial}{\partial v_z}\right]\langle f_j(\vec{v},z)\rangle\}}{\omega - k^- v_z + \Omega_j}$$

$$\equiv R_j(\vec{v},z)\ \langle f_j(\vec{v},z)\rangle \qquad (15)$$

where

$$k^+(-\omega) = k^{-*}(\omega) \text{ and } \left|\delta E^-(\omega)\right|^2 = \left|\delta E^+(-\omega)\right|^2 \qquad (16)$$

have been used (+, - refers to equation 13.), the fields are assumed axissymetric and

$$k_i << \left|\frac{\Delta[\omega - k_r(\omega)v_z]}{v_z}\right| . \qquad (17)$$

This last inequality is the usual requirement on the spectral width for the use of quasilinear theory. It can be shown that both (14) and (17) can be satisfied if the incoming ion stream is roughly a maxwellian distribution and β_i ($\beta_i \equiv \kappa T_i 8\pi n_i/B_o^2$) is sufficiently small. The turbulence is assumed weak enough so that particle trapping and mode coupling [Jackson, 1980a] can be neglected.

Equations (9), (10), (12), (13) and (15) can now be used to determine the evolution of $<f_j>$. The initial condition at $z=o^-$ on $<f_j>$ is roughly specified by figure 2. The spectrum $\delta E(z=o^-,\omega)$ must be such that $<f_j(z,\bar{v})>$ becomes marginally stable at some point, z_u, upstream where $\delta E(z_u,\omega)$ is the noise spectrum which excites the instability. $\delta E^-(o^-,\omega)$ is not actually determined in this work.

We consider the change in $<f_j>$ just upstream of $z=o^-$, far enough so that ballistic terms can be neglected, but close enough so that $<f_j(z,\vec{v})>$ can be approximated by $<f_j(o^-,\vec{v})>$ for all terms in (9) but the first. This is similar to the procedure used by Gary [1978].

The resulting equations are:

$$v_z \frac{\partial}{\partial z} < f_j(z, \vec{v}) > + \frac{q_j}{m_j} < E_z > \frac{\partial < f_j(o^-, \vec{v}) >}{\partial v_z}$$

$$= R_j(|\delta E^-|^2, \bar{v}, \omega) < f(o^-, \vec{v}) > \qquad (18)$$

$$|\delta E^{-}(z,\omega)|^2 = |\delta E^{-}(o^{-},\omega)|^2 \exp[-2k_i^{-}(o^{-},\omega)\, z] \tag{19}$$

$$D^{-}[k^{-}(o^{-},\omega),\ \omega,\ < f_j(o^{-},\ \bar{v}) >] = 0 \tag{20}$$

$$< E_z > \simeq \frac{1}{k_s^2} \sum_j 4\pi\, q_j \int d^3v\, \frac{1}{v_z}\, R_j\ < f_j(o^{-},\ \vec{v})> \tag{21}$$

$$k_s^2 \equiv 4\pi \sum_j \frac{q_j^2}{m_j} \int d^3v\ \frac{1}{v_z}\ \frac{\partial}{\partial v_z} < f_j(o^{-},\ \vec{v}) > \tag{22}$$

Equations (21) and (23) result from dividing (18) by v_z, integrating over velocity, combining the resulting equation for the density variation with (10) and assuming $k_i << k_s$.

By taking velocity moments, some insight into the effects of the turbulence on the different particle streams can be obtained. We make the following assumptions,

$$\left.\begin{aligned} \frac{c_j}{v_j} &\simeq \sqrt{\beta_i} << 1 \quad (j = u,\ r) \\ \frac{V_e}{c_e} &\simeq \frac{c_s}{c_e} = \sqrt{\frac{m_e}{m_i}} << 1 \\ \eta &<< 1 \end{aligned}\right\} \tag{23}$$

where V_j and c_j are the average velocity and thermal spread, respectively, of the jth stream(The u, r, e subscripts indicate the incoming ion, reflected ion, and electron streams). Also used are the assumptions mentioned previously, $[(\omega + \Omega_{i,e})/k_r - V_{u,e}] >> c_{u,e}$ and $|\omega| << |\Omega_e|$. Note that k_s^2 simplifies to

$$k_s^2 \simeq -\frac{1}{\lambda_{de}^2} + \frac{\omega_{pi}^2}{V_u^2} = \frac{1}{\lambda_{de}^2}\left(\frac{1 - M_a^2}{M_a^2}\right) \qquad (24)$$

$$M_a \equiv V_u/C_a$$

To get the variation in density, divide (18) by v_z, integrate, use the assumptions mentioned above, and use the dispersion relation, (20). The resulting equations are,

$$\frac{dn_u}{dz} = \frac{d}{dz}\frac{W(z)}{kT_{eo}}\frac{1}{(M_a^2 - 1)(M_a - \bar{V}_g)}\{M_a - \bar{V}_g(\frac{2}{M_r^2} - 1)\} \qquad (25)$$

$$\frac{dn_e}{dz} = \frac{d}{dz}\frac{W(z)}{kT_{eo}}\frac{1}{(M_a^2 - 1)(M_a - \bar{V}_g)}\{M_a - \bar{V}_g(\frac{2M_a^2}{M_r^2} - 1)\} \qquad (26)$$

$$\frac{dn_r}{dz} = \frac{d}{dz}\,\frac{W(z)}{kT_{eo}}\,\frac{2\bar{V}_g}{M_r^2(\bar{V}_g - M_a)}. \tag{27}$$

where,

$$W(z) \equiv \int_{-\infty}^{\infty} d\omega\, \frac{|\delta E^-(z,\omega)|^2}{4\pi}\, \frac{k_r^2 c^2}{\omega^2}$$

$$\bar{V}_g = \frac{d\omega}{dk_r} / C_a = M_a + \frac{2k_r C_a(\omega - k_r V_u + \Omega_i)^2}{\Omega_i(\omega - k_r V_u)(\omega - k_r V_u + 2\Omega_i)}$$

$$M_r \equiv V_r/C_a \approx -V_m/C_a$$

and W(z) is considered an integral operator.

Note, that equations (25) through (27) combine to insure charge neutrality. In contrast to the spacially homogeneous case, charge neutrality is not automatically satisfied by (18); it is a result of the long wavelength, low frequency characteristics of the turbulence. Particle flux is automatically conserved by (18) which leads to

$$\frac{dV_j(z)}{dz} \simeq \frac{-V_{jo}}{n_{jo}} \frac{dn_j(z)}{dz} \quad . \tag{28}$$

In order to determine the implications of (25)-(27), we assume $\bar{V}_g$ to be roughly ω independent and consider some characteristic values which occur if the ion acoustic soliton with electron trapping is used as a reflecting potential,

$$dW/dz > o,$$

$$M_a \simeq 2.8, \quad M_r \simeq 2.7, \quad \bar{V}_g \simeq M_a - 1 \; . \tag{29}$$

This last value for the group velocity is a result of examining the linear solutions for $k(\omega)$ when M_a is greater than 2.6. It is equivalent to Gary's[1978] assumption, $\omega - kV_u << \Omega;$, however this assumption was not used in arriving at (25)-(29).

It is now evident from (25)-(29) that the incoming ion stream is slowed by the turbulence as it approaches $z=o^-$ from upstream. The electron density increases in order to preserve quasi-charge neutrality. Reflected ions are slowed as they move upstream from $z=o^-$.

Further information can be obtained by investigating the momentum flux change of each j stream defined by

$$\frac{d}{dz}\Gamma_{pj} = \int d^3v\, m_j\, v_z^2\, \frac{\partial}{\partial z} < f_j(\vec{v},z) >$$

After some algebra [Jackson,1981a] we arrive at the expressions

$$\frac{d\Gamma_{pu}}{dz} \simeq -m_i V_{uo}^2 \frac{dn_u}{dz} \tag{31}$$

$$\frac{d\Gamma_{pe}}{dz} \simeq \kappa T_{eo} \frac{dn_e}{dz} \tag{32}$$

$$\frac{d\Gamma_{pr}}{dz} \simeq -m_i V_{ro}^2 \frac{dn_r}{dz} \tag{33}$$

where the density gradients represent expressions (25)-(27). The momentum flux gradients should be interpreted as the force of the turbulent whistler fields on each stream. The effect of the second order field $<E_z>$ is included as part of the medium through which the turbulent fields act on these

streams. In figure 3 the relative size of these forces is illustrated schematically for the values in (29). The vectors indicate the magnitude and direction of each species' force on the turbulent fields (which is represented by the block). Due to conservation of momentum flux, the forces combine with the inertial force of the block (the increase in field momentum flux) to equal zero. The dashed vector indicates the relative increase in field momentum flux. Note that the change in both field momentum flux and the electron momentum flux (pressure) is small relative to the change in each ion stream's momentum flux. The turbulent field therefore acts as a medium for transmission of momentum between the incoming and outgoing ion streams. This is the same conclusion which Gary [1978] made for the homogeneous time varying case. In contrast to Gary's work, an electron pressure force occurs. This force is small but not as small as the small parameters, (23).

Using equations (31)-(33) and assumptions (23), it is also possible to show that the change in the z directed velocity spread (δT_{jz}) is negligible [Jackson, 1981a].

Further information can be obtained by taking the moments,

$$\int d^3v \frac{m_j}{2} (v_\perp^2, v_\perp^2 + v_z^2) v_z \frac{\partial}{\partial z} \langle f_j(\vec{v},z) \rangle ,$$

which indicate the change in perpendicular and total energy flux of the jth species. Simplified expressions (analogous to equations (25)-(27)) have been derived in [Jackson, 1981a]. Using these expressions for the present case where the dominant unstable modes have positive group velocities, the following conclusions result:

(i) The total beam energy flux is made up of two parts, the directed beam energy flux, $n_r m_i V_r^3/2$, which decreases in magnitude moving upstream from $z=o^-$ and the perpendicular energy flux, $n_r V_r \kappa T_{\perp r}$, which increases in magnitude moving upstream from $z=o^-$. The increase in the latter more than offsets the decrease in the former to give a net increase in energy flux magnitude for the beam as it moves from $z=o^-$ to a point slightly upstream. In other words, the beam is slowed and heated while moving upstream but gains energy overall. If, in addition, the frequency of the turbulence is such that $\omega << \Omega_i$, the net gain in the total beam energy flux is much less than the change in the magnitude of the two component parts.

(ii) As the incoming ion stream moves through the turbulence in the positive $\hat{z}$ direction it's perpendicular "temperature", $T_{\perp u}$, increases and enhances the shock like character of this model. We note further that the total incoming ion energy flux decreases.

(iii) There is no change in the perpendicular temperature of the electrons ($T_{\perp e}$). However, there is a change in the total electron energy flux which decreases between $z=o^-$ and a point slightly upstream from $z=o^-$. Since there is no change in T_{ez} and $T_{\perp e}$ and since the change in directed energy is small by a mass ratio, the total electron energy is small by a mass ratio, the total electron energy flux must be a result of a change in electron heat flux. Using the previously mentioned values for $\bar{V}_g$ and M_a one can show that the change in ion energy flux is much larger (25 times) than the change in electron energy flux.

(iv) A comparison between the change in the total energy flux of the reflected beam ($d\Gamma_{wr}/dz$), the nonresonant electrons and ions ($d(\Gamma_{wu} + \Gamma_{we})/dz$), and the turbulent fields ($d\Gamma_{wf}/dz$), gives the following approximate ratios,

$$\frac{d\Gamma_{wf}}{dz} \simeq \frac{\bar{V}_g - M_a}{M_a} \cdot \frac{d(\Gamma_{wu} + \Gamma_{we})}{dz} \simeq \frac{M_a - \bar{V}_g}{\bar{V}_g} \cdot \frac{d\Gamma_{wr}}{dz}$$

Using the sample values of $\bar{V}_g$ and M_a is is evident that most of the decrease in total non resonant energy flux goes into increasing the magnitude of the total reflected beam energy flux, the remainder goes to increasing the field energy flux.

4. Conclusion

The analysis presented in the previous sections shows the plausibility of the reflected ion shock model. Using the ion acoustic soliton as a reflecting potential, the analysis indicates that this model is shock-like if M_a is large enough for downstream-moving, low frequency whistlers to occur.

A spacially varying, time independent, 2nd order theory has been formulated for the turbulence caused by the counterstreaming ions which are characteristic of this model. The pertinent results indicate that the main action of the low frequency whistler (Almost Alfven) turbulence will be to slow and scatter (in perpendicular directions) both the incoming and outgoing reflected ions. The change in turbulent field and electron momentum and energy is relatively small for large Mach numbers. There is a net loss of energy by the incoming ions which is gained by the outgoing reflected ions.

As stated previously this second order theory differs from Gary's in a number of ways. For instance, the effect of an electron pressure may be properly estimated with this type of calculation. Secondly, the expressions for gradients of density, momentum flux and energy flux are expressed in terms of quantities such a beam velocity, main ion stream

velocity and wave group velocity which are fairly easy to interpret. These expressions do not require that turbulent frequencies be much less than the ion cyclotron frequencies.

Also, this analysis considers a case where some of the ions (incoming) see a growing turbulent field and some of the ions (reflected) see a declining turbulent field. This is in contrast to the time varying homogeneous case where all particles see a growing field. In consequence, the inhomogeneous case shows a net transfer of energy from main stream ions to beam ions,whereas,in the homogeneous case, the reverse is true. Finally, the effect of the 2nd order field, in this case, is to cause the electrons to preserve quasi neutrality.

Zero group velocity modes are eliminated from this analysis by assuming Mach numbers sufficiently large (>2.6). If these modes were excited they would remain stationary and grow in time until they were large enough to cause a parametric instability [Jackson, 1980] . The resulting unstable whistler and ion acoustic waves would move downstream and further enhance shock like heating and slowing.

We note that by assuming Mach numbers greater than 2.6 it becomes possible for reflected ions to be turned around by the turbulence and to move downstream with the incoming ions. These ions are not included in this model and their effects should be the subject of further study.

4. Application to the Bow Shock

The model previously described has a number of characteristics which agree with observations of the earth's bow shock. First, there is a portion of the bow shock which can be roughly defined as parallel. This region is characterized by the occurrance of low frequency, long wavelength electromagnetic turbulence having frequencies less than or equal to the ion cyclotron frequency. This agrees with the reflected ion model if the small k instability is dominant. Secondly, backstreaming ions have been observed in the solar wind upstream from the bow shock. These ions form two types of distributions, one which is sharply peaked in energy and direction and one (which occurs most often) which has a wide spread in energy and direction. The occurrence of this last distribution and of a slowing solar wind is correlated with the observation of low frequency turbulence occurring in the same area. This agrees with the slowing and perpendicular heating described in the previous section. Also, the parameters associated with the solar wind in front of the shock are favorable to this model. Specifically; $\beta \sim 1$, $T_e/T_i > 1$, and $M_a \sim 5$. The solar wind Mach number is somewhat higher than the 3.1 upper limit for ion acoustic soliton solutions. However, this 3.1 limit may be modified by the occurrance of a number of phenomena such as Landan damping, low frequency turbulence or a local slowing of the solar wind.

Since the bow shock is rarely an exactly parallel shock, it is expected that the ion acoustic soliton (used as a model ion reflector) is modified by coupling to electromagnetic modes. In previous work [Jackson, 1981b], it was found, that, in a low beta fluid plasma, non parallel propagation results in the ion acoustic soliton becoming a short wavelength ion acoustic wavetrain superimposed on a long wavelength slow acoustic wave. For larger beta, it is expected that this long wavelength mode will become partially electromagnetic.

Recently published analysis of the two spacecraft I.S.E.E. data (June, 1981 issue J. Geophys. Res.) has made a large contribution toward describing the structure of the foreshock region just upstream from the quasiparallel bow shock. A few characteristics described by these papers are not a part of the simplified model discussed in this paper.

First of all, the bow shock is three dimensional as opposed to the one dimensional model presented here. As a result of this, some of the ions which are in front of the quasiparallel bow shock may have originally been reflected from a quasi perpendicular region and $\vec{E} \times \vec{B}$ drifted to the pre-parallel region [Bonifazi and Moreno, 1981a,b]. Ions reflected from a quasi perpendicular region can be expected

to have larger energy than those which are reflected from the quasi-parallel region [Sonnerup, 1969], [Paschmann et. al., 1980]. In addition ions reflected at the quasi perpendicular shock make up a narrow layer on the most sunward region of the foreshock [Bonifazi and Moreno, 1981a,b] and form the distribution which is classified as "reflected" (narrow, peaked distributions in energy and direction). This is in contrast to the parallel shock model presented here where one would expect the ions which are farthest upstream to be very "diffuse" (spread in energy and direction). This difference can be resolved by remembering that the outer edge of the foreshock region toughes the quasi perpendicular bow shock [Eastman et. al., 1981]. Therefore, ions reflected at this point may run along the foreshock boundary without being scattered by the highly turbulent region in front of the parallel shock.

Next, we note that the model presented here allows only very weak magnetic turbulence $|\delta B/B_o| << 1$ whereas the low frequency turbulence associated with the bow shock is quite strong ($|\delta B/B_o| \sim 1$) [Hopp et. al., 1981]. Very nonlinear waveforms have been observed. This is probably the result of allowing more reflected particles (due to larger β_i) and greater relative streaming velocity (due to larger Mach numbers and quasi-perpendicular reflection). In addition,

low frequency compressive density variations which are correlated with the low frequency electromagnetic turbulence have been detected. This may be due to nonlinear coupling [Jackson, 1980] or to slightly oblique propagation angles [Gary et. al., 1981]. One result of these strong compressive effects may be to explain the large spread in parallel velocities which is observed in the distribution of "diffuse" ions, but not predicted by the model presented in this paper. This large spread in parallel velocities permits some ions to be moving upstream without being reflected from the electrostatic barrier. It is resonant interactions with these ions which cause excitation of (in addition to right hand waves) waves which are left hand polarized in the plasma frame [Sentmann et. al., 1981].

Finally, observations by Bonifazi and Moreno [1981a,b] indicate that diffuse ions are slowed as they move upstream which is in agreement with our model. Also, they found that solar wind ions are slowed and heated by this turbulence with a net loss of total energy. This energy loss, minus a smaller increase in field energy density, is of the same order as the difference in energy between the "diffuse" and the "reflected" ion energy densities. (The total diffuse ion energy is larger than the total "reflected" ion energy density.) A possible scenario is that ions which are reflected from a quasi-perpendicular region may travel out in front

AD-A128 432 EFFECTS OF NONCONVECTIVE ELECTRIC FIELDS ON MAGNETOSPHERIC PLASMA DYNAMICS(U) NORTHEASTERN UNIV BOSTON MA M B SILEVITCH 31 JAN 83 AFOSR-TR-83-0379

UNCLASSIFIED AFOSR-78-3731 F/G 20/9 NL

2/2

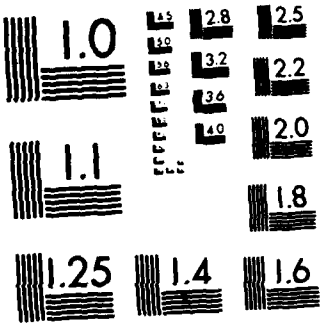

(sunside) of a region of "diffuse" ions loosing momentum and being heated. Gradually they slow enough to drift into the diffuse region in front of a more parallel shock and may then constitute a large portion of the so called "diffuse" ions. The thermal energy gained by these ions is at the expense of the solar wind kinetic energy. If this is the case, the second order analysis developed in this paper is most appropriate near the outer region of the foreshock where the ions are of the "reflected" or "intermediate" classes and where the low frequency waves have not become extremely large and nonlinear.

In conclusion, our reflected ion shock model seems to agree qualitatively with a number of bow shock observations. However, the three dimensional characteristics of the bow shock and its large shock strength add effects which must be the subject of future research.

Barnes, A., Theory of generation of bow shock associated hydromagnetic waves in the upstream interplanetary medium, Cosmic Electrodynamics, 1, 90, 1970.

Biskamp, D. and H. Welter, Structure of the earth's bow shock, J. Geophys. Res., 77, 6052, 1972.

Bonifazi, C. and Moreno, G., Reflected and diffuse ions backstreaming from the earth's bow shock 1. Basic Properties, J. Geophys. Res., 86, 4397, 1981.

Bonifazi, C. and Moreno, G., Reflected and diffuse ions backstreaming fron the earth's bow shock 2. Origin, J. Geophys. Res., 86, 4405, 1981.

Eastman, T. E., R. R. Anderson, L. A. Frank, and G. K. Parks, Upstream particles observed in the earth's foreshock region, J. Geophys. Res., 86, 4379, 1981.

Gary, S. P., The electromagnetic ion beam instability and energy loss of fast alpha particles, Nucl. Fusion, 18, 327, 1978.

Gary, S. P. and W. C. Feldman, A second order theory for $k||B_o$ electromagnetic instabilities, Phys. Fluids., 21, 1980.

Gary, S. P., J. T. Gosling and D. W. Forslund, The electromagnetic ion beam instability upstream of the earth's bow shock, J. Geophys. Res., 86, 6691, 1981.

Hoppe, M. M., C. T. Russell, L. A. Frank, T. E. Eastmann, and E. W. Greenstadt, Upstream hydromagnetic waves and their association with backstreaming ion populations: I. S. E. E. 1 and 2 observations, J. Geophys. Res., 86, 4471, 1981.

Jackson, R. W. and K. I. Golden, Formation of precursor whistler mode plasma turbulence in parallel shock waves, J. Plasma Phys., 22, 491, 1979.

Jackson, R. W., Parametric instability due to a low frequency whistler wave, Phys. Lett. A, 77A, 438, 1980.

Jackson, R. W., A collisionless plasma shock model and related nonlinear effects, Ph. D. thesis, Northeastern University, Boston, MA, 1981.

Jackson, R. W., Nonlinear electrostatic waves: oblique propogation, J. Plasma Phys., 26, 399, 1981.

Kennel, C. F. and R. Z. Sagdeev, Gollisionless shock waves in high β plasmas, 1, J. Geophys. Res. 72, 3303, 1967.

Lindman, E. L. and W. E. Drummond, Studies of oblique shock structure, report, University of Texas Austin Texas, 1971.

Passchmann, G., N. Sckopke, R. Asbridge, S. J. Bame, J. T. Gosling, Energization of solar wind ions by reflection from the earth's bow shock, J. Geophys. Res., 85, 4689, 1980.

Sentmann, D. D., J. P. Edmiston, L. A. Frank, Instabilities of low frequency, parallel propagating electromagnetic waves in the earth's foreshock region, J. Geophys. Res., 86, 6691, 1981.

Sonnerup, B. U. O., Acceleration of particles reflected at a shock front, J. Geophys. Res., 74, 1301, 1969.

Figure Captions

Figure 1. Schematic of reflecting ion shock model.

Figure 2. Ion distribution at $z = o^{-}$.

Figure 3. Schematic for momentum flux balance. Dashed line indicates change in field momentum flux.

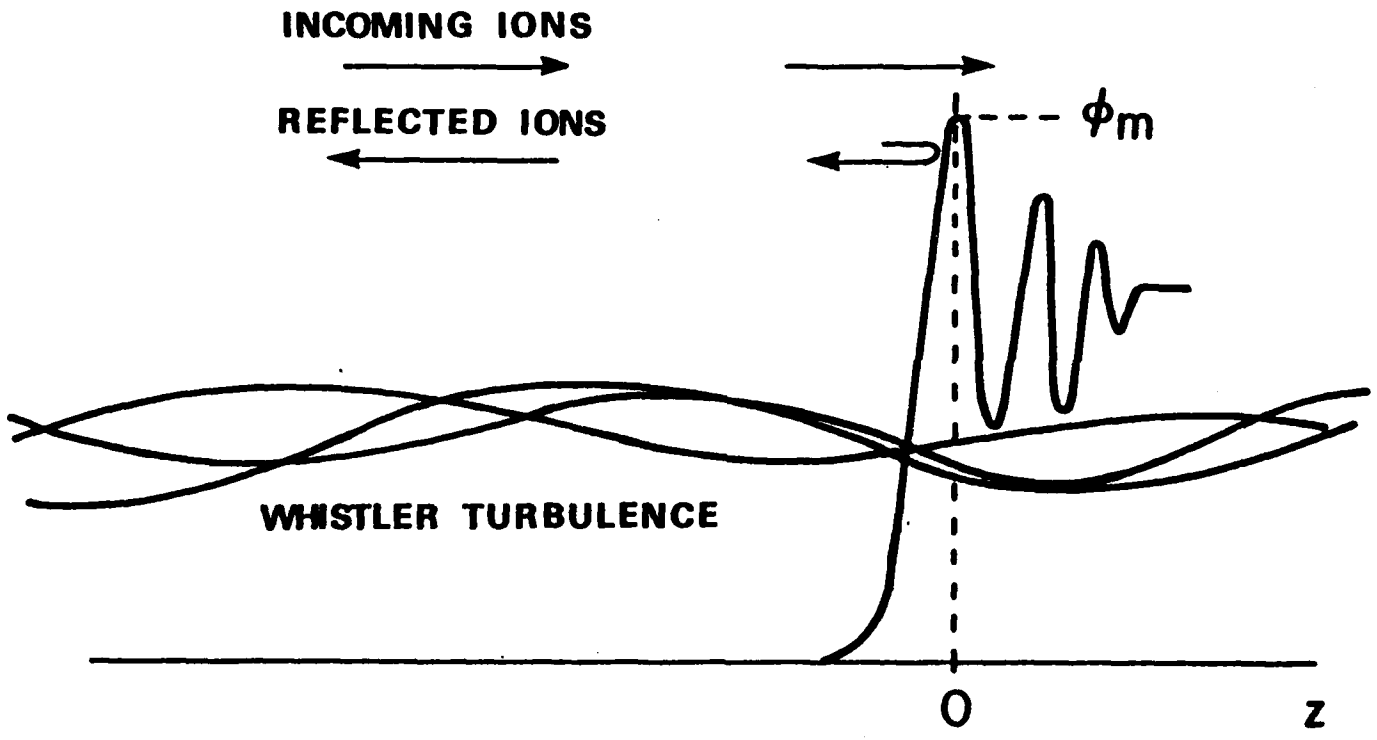

FIGURE 1.

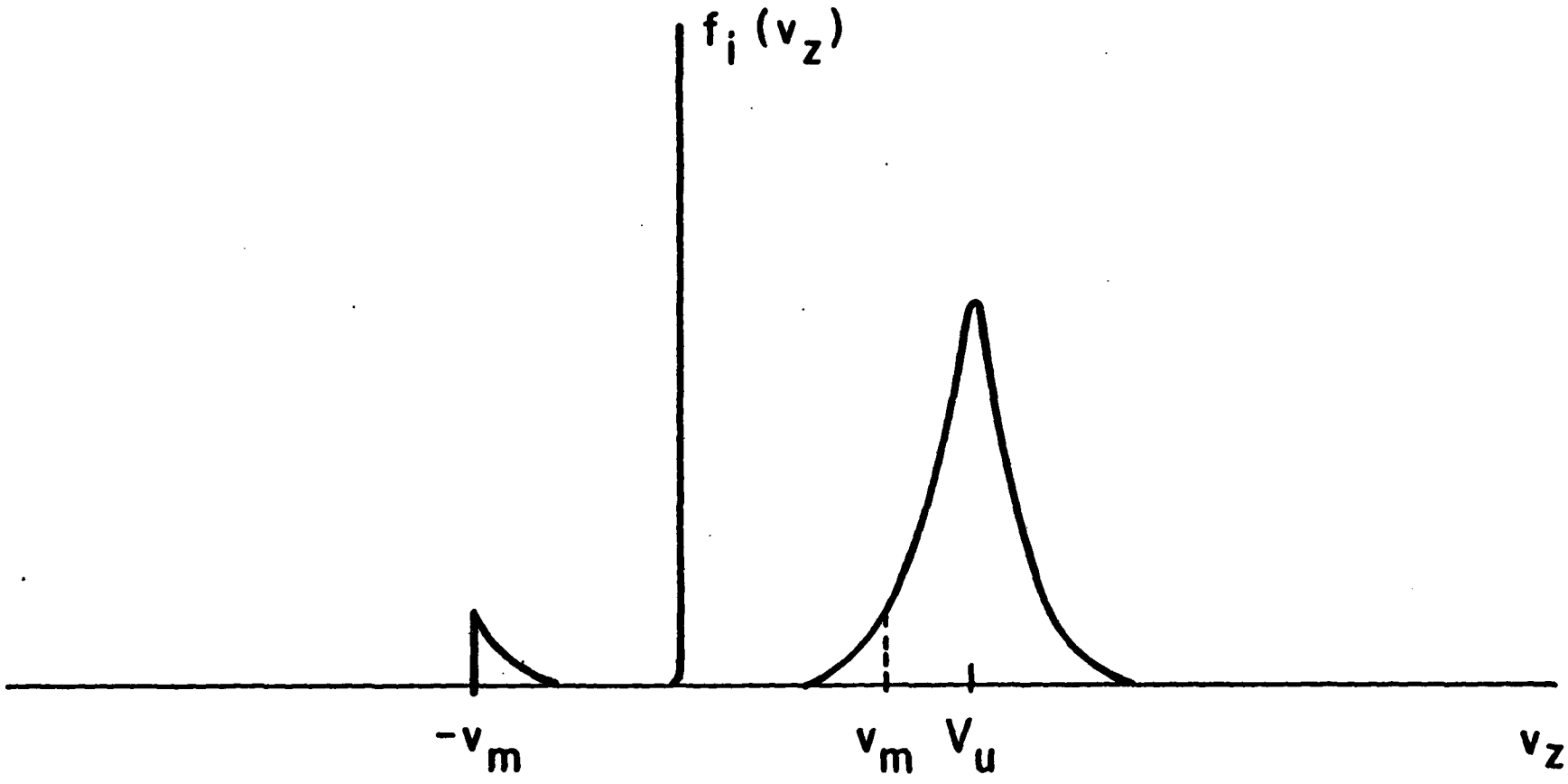

FIGURE 2.

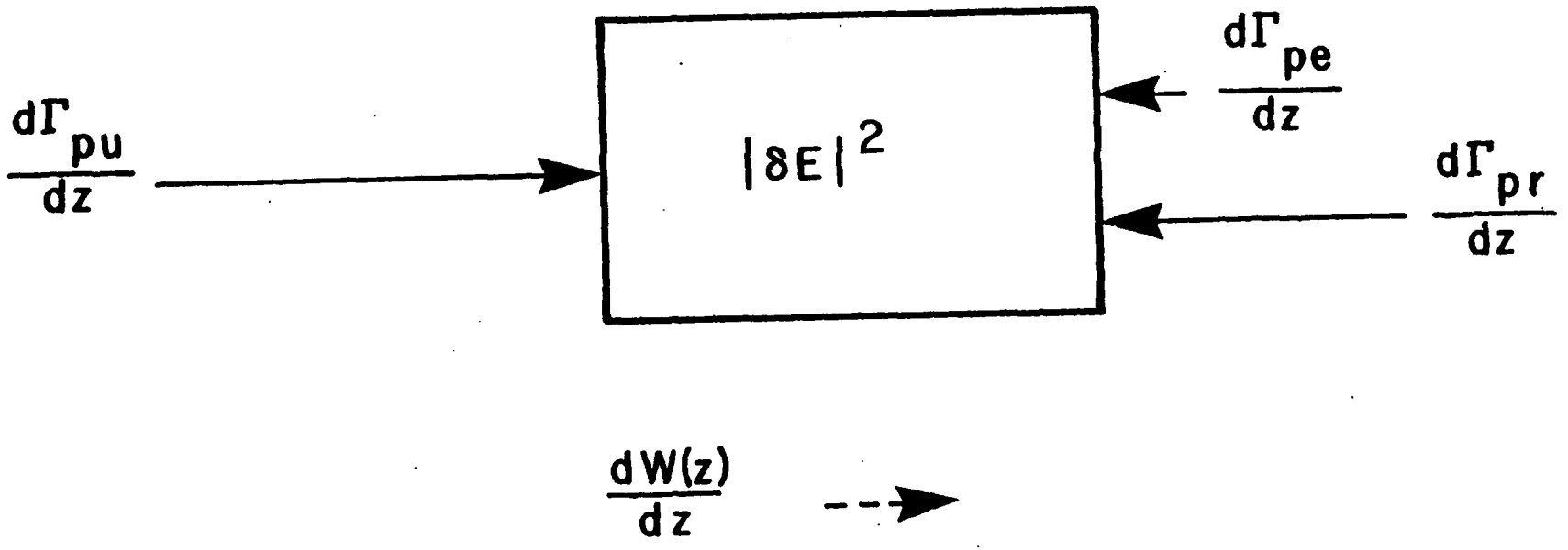
$\frac{d\Gamma_{pu}}{dz}$
$|\delta E|^2$
$\frac{d\Gamma_{pe}}{dz}$
$\frac{d\Gamma_{pr}}{dz}$
$\frac{dW(z)}{dz}$

FIGURE 3.


MEI
8